

---

# QCPINN: QUANTUM-CLASSICAL PHYSICS-INFORMED NEURAL NETWORKS FOR SOLVING PDES

---

Afrah Farea<sup>1</sup>, Saiful Khan<sup>2</sup>, Mustafa Serdar Celebi<sup>1</sup>

<sup>1</sup>Computational Science and Engineering Department, Informatics Institute  
Istanbul Technical University, Istanbul 34469, Turkiye  
farea16@itu.edu.tr, mscelebi@itu.edu.tr

<sup>2</sup>Scientific Computing, Rutherford Appleton Laboratory  
Science and Technology Facilities Council (STFC), OX11 0QX, United Kingdom  
saiful.khan@stfc.ac.uk

## ABSTRACT

Physics-informed neural networks (PINNs) have emerged as promising methods for solving partial differential equations (PDEs) by embedding physical laws within neural architectures. However, these classical approaches often require a large number of parameters to achieve reasonable accuracy, particularly for complex PDEs. In this paper, we present a quantum-classical physics-informed neural network (QCPINN) that combines quantum and classical components, allowing us to solve PDEs with significantly fewer parameters while maintaining comparable accuracy and convergence to classical PINNs. We systematically evaluated two quantum circuit architectures across various configurations on five benchmark PDEs to identify optimal QCPINN designs. Our results demonstrate that the QCPINN achieves stable convergence and comparable accuracy, while using only 10-30% of the trainable parameters required by classical PINNs. This approach also results in a significant reduction in the relative  $L_2$  error for Helmholtz, Klein-Gordon, and Convection-diffusion equations, with reduction ranging from 4% to 64% across various fields. These findings demonstrate the potential of parameter efficiency and solution accuracy in physics-informed machine learning, allowing for a substantial decrease in model complexity without compromising solution quality. QCPINN presents a promising pathway to address the computational challenges associated with solving PDEs.

## 1 Introduction

Recent advancements in machine learning have transformed approaches to solving partial differential equations (PDEs), with Physics-informed neural networks (PINNs) emerging as an innovative technique. PINNs embed physical laws directly into neural network architectures, eliminating the need for labeled training data while strictly enforcing physical constraints. This approach has demonstrated considerable success in modeling various physical phenomena across scientific and engineering domains [1, 2, 3, 4]. Although they hold great potential, research is underway to improve the accuracy of PINNs in modeling different PDEs and physical systems. They often encounter challenges with stiff systems, capturing steep gradients, and efficiently navigating high-dimensional parameter spaces for reasons such as memory requirements, slow convergence, or when calculating high-order or high-dimensional derivatives [5, 6]. While increasing model expressivity through additional parameters can alleviate these challenges, this approach introduces new problems: increased computational cost, risk of overfitting, and unstable convergence behavior during training [7, 8]. Such a trade-off between model complexity, generalization, and convergence ability is a fundamental challenge in neural network design.

Quantum computing presents a promising paradigm for overcoming these limitations. With its ability to process high-dimensional data and exploit quantum principles such as superposition and entanglement, quantum algorithms offer unique advantages for solving complex computational problems. For instance, the Harrow-Hassidim-Lloyd (HHL) algorithm has demonstrated theoretical exponential speedups for specific linear systems, while variational quantum

algorithms provide practical near-term solutions [9, 10, 11]. Moreover, recent developments [12, 13, 14, 15] indicate that quantum neural networks possess an expressive power that could significantly enhance the learning capabilities for modeling complex physical systems.

Although both PINNs and quantum computing have advanced independently, their integration remains largely unexplored. Several preliminary efforts have emerged: Sedykh et al. proposed HQPINN [16], focusing on computational fluid dynamics in 3D Y-shaped mixers; Dehaghani et al. introduced QPINN [17], integrating a dynamic quantum circuit with classical computing methodologies for optimal control problems; Trahan et al. [18] investigated both purely quantum and hybrid PINNs. Leong et al. proposed HQPINN [19], which is inspired by Fourier neural operators. However, existing research has not comprehensively established whether quantum-enhanced models can improve upon purely classical PINNs across a broad range of PDEs efficiently and reliably.

We investigate the limitations of traditional PINNs by integrating quantum computing circuits with classical neural networks. We propose that such a hybrid approach can leverage complementary strengths: classical computing’s robustness and quantum computing’s enhanced expressivity with inherent parallelism. We believe this method will allow us to solve a wide range of PDEs with similar or better accuracy while requiring significantly fewer trainable parameters than classical models.

To this end, we introduce a hybrid architecture named Quantum-Classical Physics-Informed Neural Network (QCPINN). To search for a suitable QCPINN architecture and its configurations, we systematically evaluate multiple dimensions of the design space: two quantum circuit architectures: (a) discrete-variable (DV) qubit-based circuits with configurations, such as four circuit topologies: Alternate, Cascade, Cross-mesh, and Layered; and two embedding schemes: Amplitude and Angle; (b) continuous-variable (CV) circuits with configurations, including two measurement schemes: number and quadrature; three nonlinear operations: Kerr, cubic phase, and cross-Kerr; and two parameterizations: phase-free (magnitude) and full (magnitude and phase). We evaluate the performance of these QCPINN models across various PDEs, such as the Helmholtz and lid-driven Cavity equations, while also extending our analysis to the Klein-Gordon, Wave, and Convection-diffusion equations. Our comprehensive assessment compares (a) solution accuracy, (b) convergence rates, (c) parameter efficiency (d) time, and (f) memory between classical PINNs and QCPINN variants.

To ensure reproducibility and facilitate collaborative advancement, we have made all components of QCPINN open-source code and publicly available on GitHub at <https://github.com/afrah/QCPINN> [20].

## 2 Related Work

In the domain of PDE solvers, quantum algorithms can be broadly categorized into two primary approaches: (a) exclusively quantum algorithms and (b) hybrid quantum-classical methods.

### 2.1 Exclusively Quantum Algorithms

Exclusively quantum algorithms for solving PDEs typically leverage unitary operations and quantum state embedding techniques to achieve a computational advantage. In contrast to neural networks, exclusively quantum algorithms use fixed quantum circuit structures with no trainable parameters. The celebrated Harrow-Hassidim-Lloyd (HHL) algorithm is an example of this category, which provides exponential speedups to solve linear systems under specific conditions [21]. Extensions of the HHL algorithm have been applied to solve sparse linear systems derived from discretized linear [22, 23] or nonlinear [24] PDEs, leveraging numerical techniques such as linear multistep method [25], Chebyshev pseudospectral method [26], and Taylor series approximations [27]. In fluid dynamics applications, lattice-gas quantum models have been examined for directly solving PDEs [28, 29] or PDEs derived from ODEs through methods such as the Quantum Amplitude Estimation Algorithm (QAEA) [30, 31].

Despite these advancements, purely quantum algorithms for solving PDEs encounter practical challenges such as requirements for quantum error correction [32, 33, 34], limitations in circuit depth [35, 29, 36], and bottlenecks in classical data embedding [37, 38, 39]. These obstacles, among others, limit the near-term viability of exclusively quantum PDE solvers on today’s noisy intermediate-scale quantum (NISQ) devices.

### 2.2 Hybrid Quantum-Classical Approaches

Hybrid quantum-classical approaches have emerged as promising solutions to overcome the limitations of exclusively quantum algorithms. These methods combine the nonlinearity, maturity, and stability of classical computation with the enhanced capacity, expressivity, and inherent parallelism of quantum systems. While classical components can efficiently handle pre-/post-processing, optimization, and error stabilization, quantum layers can capture intricate patterns, solve sub-problems, and accelerate specialized computations.

Within this hybrid paradigm, Quantum Neural Networks (QNNs), also referred to as parameterized quantum circuits (PQC), have demonstrated universal approximation capabilities for continuous functions when implemented with sufficient depth, width, and well-designed quantum feature maps. For instance, Salinas et al. [40] showed that single-qubit networks with iterative input reuploading can approximate bounded complex functions, while Goto et al. [41] established universal approximation theorems for quantum feedforward networks. Schuld et al. [13] revealed that the outputs of parameterized quantum circuits (with suitable data embedding and circuit depth) can be expressed as truncated Fourier series, thereby providing theoretical support for the universal approximation ability of QNNs. Liu et al. [42] provided formal evidence of quantum advantage in function approximation. Killoran et al [43] demonstrate the universality of the continuous variable quantum models by showing that many classical neural networks can be effectively emulated on a photonic quantum computer. These developments not only support applications in solving PDEs and optimization tasks but also extend to other computational tasks such as quantum chemistry [44], material sciences [45, 46], and pattern recognition [47], to name a few.

A well-known example of this integrated approach is the Variational Quantum Algorithms (VQA) or Variational Quantum Circuits (VQC). These algorithms employ parameterized quantum circuits with tunable gates optimized through classical feedback loops. VQA implementations for solving PDEs include the Variational Quantum Eigensolver (VQE) [48, 49], Variational Quantum Linear Solver (VQLS) [50], and Quantum Approximate Optimization Algorithm (QAOA) [51], as well as emerging methods like Differentiable Quantum Circuits (DQCs) [52, 53], quantum kernel methods [54], and Quantum Nonlinear Processing Algorithms (QNPA) [55].

The aforementioned methods primarily utilize qubit-based quantum computing, which represents the predominant paradigm in quantum computing literature. However, continuous-variable quantum computing (CVQC) [56] offers an alternative computational model that leverages continuous degrees of freedom, such as quadratures and electromagnetic field momentum. For consistency, we refer to qubit-based models as discrete-variable (DV) circuit models throughout this work.

Recently, VQA have been extended to Physics-informed quantum neural networks (PIQNN) [57, 17, 18, 16, 19], broadening their applicability across physics and engineering domains. These hybrid methods offer several distinct advantages when implemented within the PINN framework.

Firstly, these models enable the flexible configuration of inputs and outputs independent of qubit/qumode counts or quantum layer depth, making them particularly effective for scenarios where the input dimension (e.g., temporal and spatial coordinates) differs from output dimensions (e.g., dependent variables like velocity, pressure, and force). Secondly, hybrid approaches facilitate increased trainable parameter counts without the need for deeper quantum circuits, additional qubits, or higher cutoff dimensions in CV quantum systems. These factors are particularly crucial in the NISQ era, where hardware constraints impose strict limits on circuit depth and coherence times, making deeper quantum networks computationally expensive and impractical [58, 59]. Thirdly, these qualities are especially advantageous for PINNs, where shallow network architectures are favored to optimize the balance between computational efficiency and solution accuracy [60, 61, 62, 8]. Finally, a substantial benefit of such hybrid models is the integration of automatic differentiation within both classical and quantum networks. This capability, supported by contemporary software packages like PennyLane [63] and TensorFlow Quantum [64], enables the automatic computation of derivatives as variables are directly incorporated into the computational graph. This approach simplifies PINN implementation and facilitates the efficient handling of complex physics-informed loss functions and higher-order derivatives.

Our work is related to the approaches in [16, 17, 18, 19], but with several key differences. While HQPINN [16] focuses specifically on computational fluid dynamics in 3D Y-shaped mixers using a fixed quantum depth with an infused layer structure, the QPINN [17] integrates a dynamic quantum circuit combining Gaussian and non-Gaussian gates with classical computing methodologies to solve optimal control problems. In addition, the model proposed in [18] investigates both purely quantum and hybrid PINNs, highlighting parameter efficiency but relying on limited PQC networks and addressing primarily simple PDEs. Recently proposed HQPINN [19], inspired by the Fourier neural operator (FNO) [65], introduces a parallel hybrid architecture to separately model harmonic and non-harmonic features before combining them for the output. The present work addresses general PDE solving with multiple quantum circuit configurations and explicit emphasis on parameter efficiency.

### 3 Background

#### 3.1 Physics Informed Neural Network (PINNs)

In the present work, we consider a general partial differential equation of the form:

$$\begin{aligned} \mathcal{D}[u(\mathbf{x}); \alpha] &= f(\mathbf{x}), \quad \mathbf{x} \in \Omega, \\ \mathcal{B}_k[u(\mathbf{x})] &= g_k(\mathbf{x}), \quad \mathbf{x} \in \Gamma_k \subset \partial\Omega, \quad k = 1, 2, \dots, n_b \end{aligned} \quad (1)$$

where,  $\mathcal{D}$ ,  $\mathcal{B}_k$  denote arbitrary differential and boundary/initial operators, respectively. The term  $f(\mathbf{x})$  refers to the source term or forcing function in the PDE. The functions  $g_k(\mathbf{x})$  refer to a set of boundary/initial functions,  $\alpha$  is a set of parameter vector or coefficient and  $u(\mathbf{x})$  is the solution of the differential equation given input  $\mathbf{x}$  in the solution domain  $\Omega$  with boundary  $\partial\Omega$ .

PINNs [66] provide a framework to embed governing physical laws directly into neural network architectures. The PINN loss function combines terms representing governing equations and initial/boundary conditions designed to minimize deviations from physical laws. More formally, the PINN loss function can be defined as:

$$\begin{aligned} \mathcal{L}(\theta) &= \arg \min_{\theta} \sum_{k=1}^n \lambda_k \mathcal{L}_k(\theta) \\ &= \arg \min_{\theta} \left( \lambda_1 \mathcal{L}_1(D[u_{\theta}(\mathbf{x}); \alpha] - f(\mathbf{x})) + \sum_{k=2}^{n_b} \lambda_k \mathcal{L}_k(B[u_{\theta}(\mathbf{x})] - g_k(\mathbf{x})) \right), \end{aligned} \quad (2)$$

where,  $n_b$  denotes the total number of loss terms,  $\mathcal{L}_k$  are the individual loss functions for each constraint with weighting coefficients  $\lambda_k$ , and  $\theta$  represents the trainable parameters.

While the initial and boundary conditions guarantee a unique solution by satisfies predefined constraints at specific spatial or temporal locations, the physics loss acts as a regularizer, guiding the network to learn physically consistent solutions and preventing overfitting to sparse or noisy data. The balance between these loss components is crucial for achieving accurate solutions, as improper weighting can lead to underfitting the initial/boundary conditions or failing to capture the system dynamics correctly. In the present work adopts soft imposition of the boundary and initial conditions using fixed weights with the best empirical results. However, various weighting methods have been proposed in the literature using different criteria, such as gradient information [67, 68, 69], loss-term history statistics [70, 71], training dataset information [72, 73, 74], or hard imposition of initial and boundary conditions [75, 76], to name a few.

#### 3.2 Continuous Variable (CV) QNN

In photonic quantum computing, CV computation addresses quantum states with continuous degrees of freedom, such as the position ( $x$ ) and momentum ( $p$ ) quadratures of the electromagnetic field. Within this framework, qumodes represent the fundamental units of the CV quantum systems, analogous to qubits in discrete-variable systems. Unlike qubits, qumodes encode information in the continuous degrees of freedom of electromagnetic field modes, rather than discrete two-level states. The computational space is, in principle, unbounded, involving infinite-dimensional Hilbert spaces with continuous spectra. To make these simulations computationally feasible, a cutoff dimension is employed to limit the number of basis states used for approximation. The computational state space is defined as  $r = m^n$ , with  $n$  qumodes and cutoff dimension  $m$ . For example, with three qumodes and a cutoff dimension of 2, the state space is 8-dimensional. Ideally, higher cutoff dimensions (up to a certain threshold) yield more precise results but at the cost of increased computational complexity.

In this work, we adhere to the affine transformation introduced in [43]. The proposed circuit ansatz consists of a sequence of operations that manipulate quantum states in the phase space. Each layer of the CV-Circuit QNN includes the following key components:

1. **Interferometers** ( $U_1(\psi_1, \phi_1)$  and  $U_2(\psi_2, \phi_2)$ ): Linear optical interferometers perform orthogonal transformations, represented by symplectic matrices. These transformations adjust the state by applying rotation and mixing between modes, corresponding to beam splitting and phase-shifting operations.
2. **Squeezing Gates** ( $S(r, \phi_s)$ ): These gates scale the position and momentum quadratures independently, introducing anisotropic adjustments to the phase space. Encoding sharp gradients using squeezing gates is particularly appealing for PDE solvers, as it allows fine-tuning of local characteristics [16].

3. **Displacement Gates** ( $D(\alpha, \phi_d)$ ): These gates shift the state in phase space by adding a displacement vector  $\alpha$ , translating the state globally without altering its internal symplectic structure.
4. **Non-Gaussian Gate** ( $\Phi(\lambda)$ ): To introduce nonlinearity, a non-Gaussian operation, such as a cubic phase, Kerr, and cross-Kerr gates, is applied. This step enables the neural network to approximate nonlinear functions and enhances the ability to solve complex, nontrivial PDEs.

These components together mimic the classical affine transformation such that:

$$L(|x\rangle) = |\Phi(Mx + b)\rangle = \Phi(D \circ U_2 \circ S \circ U_1), \quad (3)$$

where,  $M$  represents the combined symplectic matrix of the interferometers and squeezing gates,  $x$  is the input vector in the phase space,  $b$  is the displacement vector with nonlinear transformation  $\Phi$ .

In addition to the building blocks above, CV-Circuit QNNs offer flexibility in measurement schemes and parameterization strategies. Measurement can be performed in either the number basis, which projects the state onto discrete photon-number states, or the quadrature basis, which yields continuous-valued outcomes corresponding to position or momentum observables. The parameterization of unitary operations may either be full (including both magnitude and phase) or restricted to magnitude-only (by setting phase parameters  $\phi$  to zero), which can improve trainability and mitigate optimization challenges at the cost of reduced expressivity.

Although such a model exhibits intriguing theoretical properties, their practical implementation in real-world problem solving seems to suffer from fundamental stability issues. This is mainly due to their inherent sensitivity and reliance on continuous degrees of freedom, which complicate optimization compared to DV-based approaches (discussed in detail in section 3.3). This sensitivity stems from several factors, including the precision required for state preparation, noise from decoherence, and the accumulation of errors in variational quantum circuits. Furthermore, the transformations involved in CV quantum circuits are prone to numerical instabilities, particularly when optimized using gradient-based methods. Although foundational studies about the barren plateau problem, such as [77, 78, 79], primarily address DV circuit systems, the analysis indicates that similar issues can arise in CV quantum systems. In particular, the infinite-dimensional Hilbert space and the continuous nature of parameterization can exacerbate the barren-plateau effects.

### 3.3 Discrete Variable (DV) QNN

DV-Circuit quantum models do not inherently provide affine transformations as a core feature like CV-based QNNs discussed in 3.2. However, they can achieve affine-like behaviour through parameterized single-qubit rotations, controlled operations, and phase shifts for amplitude adjustments. Therefore, the affine transform of equation (3) can be reinterpreted to align with their architecture such that:

1.  **$Mx + b$** : can be achieved through a combination of parameterized quantum gates:
  - $U_1, U_2$ : A unitary operator that can be represented by parameterized single-qubit rotations, such as  $RX(\theta)$ ,  $RY(\theta)$ , or  $RZ(\theta)$ .
  - $S$ : A sequence of controlled gates (e.g., CNOT or CZ) responsible for introducing entanglement, which enables the representation of correlated variables and interactions.
  - $D$ : Data encoding circuits that map classical data into quantum states through techniques such as basis embedding, amplitude embedding, or angle embedding.
2. **Non-linear Activation** ( $\Phi$ ): DV-Circuit QNNs lack intrinsic quantum nonlinearity due to the linearity of quantum mechanics. However, classical measurements or a combination of classical measurements and non-linear activation functions (such as Tanh) can be applied to the output between quantum layers [80, 81].

## 4 Quantum-Classical Physics-Informed Neural Networks (QCPINN)

Fig. 1 illustrates a high-level overview of our proposed QCPINN architecture. The preprocessor consists of a two-layer classical neural network. The first layer performs a linear transformation to modify the input dimension, followed by a nonlinear activation function to introduce classical non-linearity. The second layer subsequently maps the transformed inputs to the QNN layer (or classical NN layer used for comparison). The postprocessor layer mirrors the structure of the preprocessor, maintaining consistent dimensions and ensuring a symmetric transformation between classical and quantum representations. This design provides flexibility in encoding classical inputs to quantum inputs and decoding quantum outputs back to classical outputs. Additionally, it manages input-output dimensions and regulates quantum feature representations, all while ensuring the higher-order differentiability necessary for residual loss in the proposed QCPINN model.

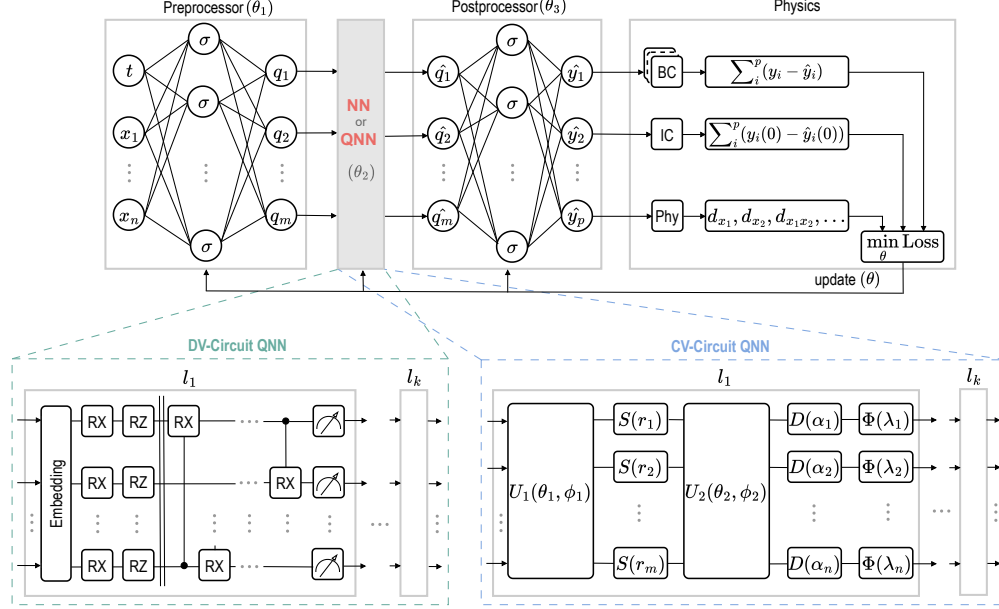


Figure 1: Overview of the proposed QCPINN architecture, illustrating its hybrid structure consisting of three main components: (a) a classical preprocessor for input encoding, (b) the core processing unit using either a quantum neural network (QNN) or classical neural network (NN), and (c) a classical postprocessor for decoding the QNN or NN outputs. The QNN is implemented as either a CV or DV circuit with  $k$  layers. The architecture integrates a loss function to concurrently minimize PDE residuals and enforce compliance with initial and boundary conditions, thereby ensuring adherence to physical constraints during training. The various configurations of the CV and DV circuits are detailed in Table 1.

Table 1: Various configurations of the QCPINN, along with the list of PDEs used for testing. Each configuration was evaluated against the Helmholtz and lid-driven Cavity cases, with the top-performing setups subsequently selected for further assessment on additional scenarios, including Wave, Klein-Gordon, and Convection-diffusion problems.

QNN	Configurations		PDEs
	Type	Options	
CV-Circuit	Measurement schemes	Number, Quadrature	<i>(tested on all configurations)</i> Helmholtz, Lid-driven Cavity
	Nonlinear operations	Kerr, Cubic phase, Cross-kerr	
	Parameterization	Phase-free (magnitude), Full (magnitude and phase) (see Algorithm 1)	<i>(tested on selected configurations)</i> Wave, Klein-Gordon, Convection-diffusion
DV-Circuit	Embeddings	Amplitude, Angle	
	Topology	Alternate, Cascade, Cross-mesh, Layered (see Fig. 2 and Table 2)	

#### 4.1 CV-Circuit QCPINN

The CV-Circuit QCPINN consists of three primary components: a classical preprocessor network, a CV-Circuit quantum network (the QNN layer of Fig. 1), and a classical postprocessor network. The quantum network is adapted from [43] and is described in Algorithm 1. Each layer of the quantum network executes a sequence of quantum operations.

Table 1 presents various configurations of our CV-Circuit studied to identify a suitable parameterization scheme, nonlinear operation, and measurement approach. For measurement schemes, we evaluated both number and quadrature. For parameterization, we examined phase-free using only magnitude parameters and full parameterization using both magnitude and phase parameters. For nonlinear operations, we explored Kerr nonlinearity, cubic phase gates, and cross-Kerr interactions. Additionally, the quantum state is measured, typically in either the quadrature basis  $\langle \hat{q}_i \rangle$  or the Fock number basis  $\langle \hat{n}_i \rangle$ , to yield classical outputs for the postprocessing layers. Please refer to section 3.2 for additional details.

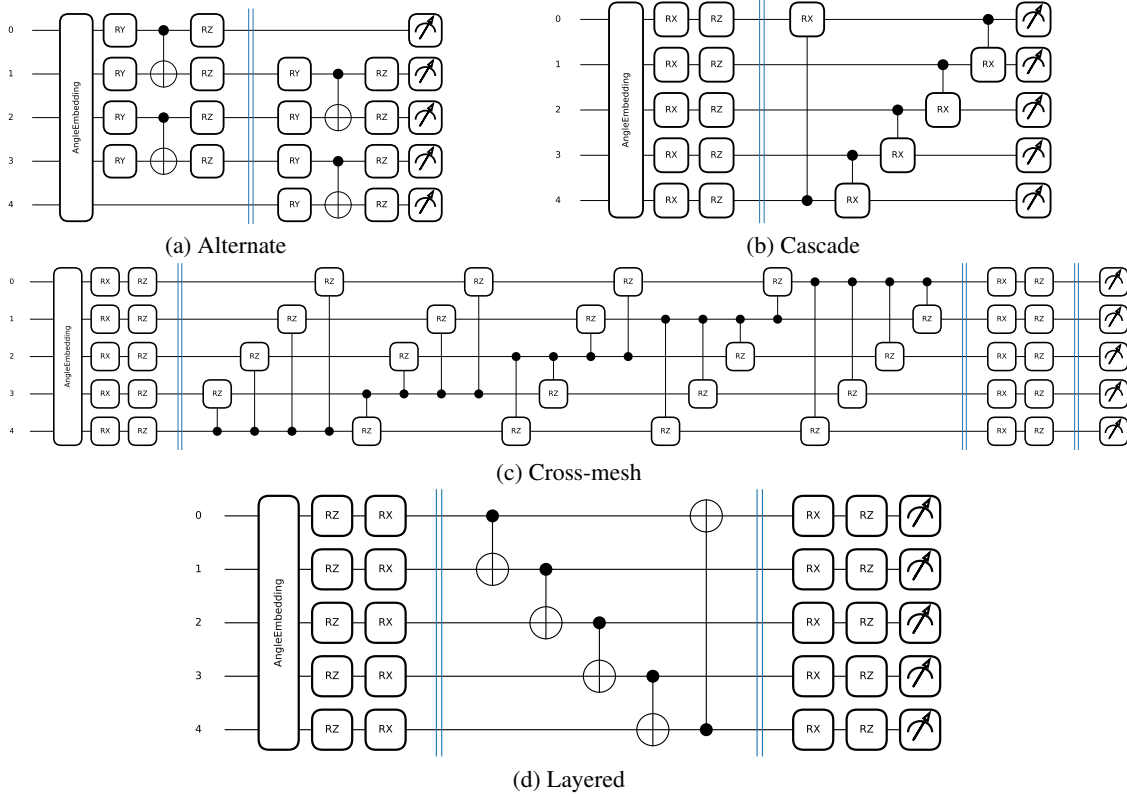


Figure 2: DV-Circuit topologies evaluated in this study, shown with five qubits and angle embedding as an example. Square boxes denote parameterized single-qubit rotation gates, and lines with dots indicate entangling operations (e.g., CNOT gates). The characteristics of these circuits are shown in Table 2.

Table 2: Characteristics of the topologies used in DV-Circuits in Fig. 2, where  $n$  is the number of qubits, and  $L$  is the number of layers.

Topology	Circuit Depth	Circuit Connectivity	Number of Parameters	Number of two-qubit gates
Alternate	$6L$	Nearest-neighbor	$4(n-1)L$	$(n-1)L$
Cascade	$(n+2)L$	Ring topology	$3nL$	$nL$
Cross-mesh	$(n^2 - n + 4)L$	All-to-all	$(n^2 + 4n)L$	$(n^2 - n)L$
Layered	$6L$	Nearest-neighbor	$4nL$	$(n-1)L$

Structuring the network in this way results in a circuit depth of  $(2n+3)L$ , while the number of trainable quantum parameters increases to  $\mathcal{O}(n^2L)$ , with  $n$  qumodes and  $L$  number of layers.

## 4.2 DV-Circuit QCPINN

Similar to the QCPINN (CV-Circuit) discussed in 4.1, the DV-Circuit QCPINN consists of three primary components: a classical preprocessor network, a quantum network (the QNN layer of Fig. 1), and a classical postprocessor network. The quantum network is a custom DV-Circuit, which executes quantum operations on the preprocessed data. Table 1 presents various configurations of our DV-Circuit studied to identify a suitable embedding scheme and topology. Fig. 2 illustrates four proposed ansätze named after their topology: Alternate, Cascade, Cross-mesh, and Layered. These circuits are adapted from literature, including [82, 83, 84, 57]. All square boxes in the figure denote parameterized single-qubit or controlled-rotation gates (RX, RY, RZ, CRX, CRZ), which are optimized during training.

Table 2 presents features of the DV-Circuits across the key descriptors, circuit depth, connectivity, number of parameters, and the number of two-qubit gates. Here, circuit depth refers to the longest computational path in the circuit from the data input to the output, which represents the maximum number of logically dependent gates executed on a single qubit. This metric is critical as deeper circuits require more computational resources and may incur numerical errors that can

degrade gradient quality during neural network optimization. The chosen circuits agree with the affine transformation discussed in section 3 and adhere to the hardware-efficient ansatz (HEA) [85] defined as:

$$U(\psi) = \prod_k U_k(\psi_k) W_k, \quad (4)$$

where, each layer  $k$  alternates between single-qubit parameterized rotations,  $U_k(\psi_k)$ , and an entangling operation,  $W_k$ .

The **Cross-mesh** ansatz implements an all-to-all connectivity scheme, facilitating extensive interaction between qubits, which enhances its ability to explore the Hilbert space. The circuit depth scales as  $\mathcal{O}(n^2 - n + 4)L$ , while the number of trainable parameters is  $(n^2 + 4n)L$ . The use of global entanglement fosters strong correlations between qubits; however, it results in larger circuit depth, resource demands, and training difficulties [79]. This circuit’s total number of two-qubit gates is also significantly higher than in other ansätze.

The **Cascade** ansatz balances expressivity and hardware efficiency by employing a ring topology for qubit connectivity. This design facilitates efficient entanglement while keeping the circuit depth manageable at  $(n + 2)L$ . The circuit contains  $3nL$  trainable parameters, making it more efficient than Cross-mesh while maintaining reasonable expressivity. Incorporating controlled rotation gates ( $CRX$ ) improves entanglement compared to CNOT gates and increases the circuit’s capacity to explore the Hilbert space. Furthermore, the requirement for two-qubit gates is fewer than that of Cross-mesh, thus lowering the overall computational cost.

The **Layered** ansatz features a structured design that includes alternating rotation and entangling layers. Each qubit undergoes parameterized single-qubit rotations, typically utilizing  $RX$  and  $RZ$  gates. Entanglement is achieved through nearest-neighbor CNOT gates. Compared to the Cross-mesh’s all-to-all connectivity or the Cascade’s ring topology, the Layered architecture represents a compromise between expressivity and hardware efficiency.

Among the evaluated DV topologies, the Alternate ansatz employs alternating layers of parameterized single-qubit rotations followed by nearest-neighbor CNOT gates, ensuring effective entanglement while maintaining a manageable circuit depth of  $6L$  and  $4(n - 1)L$  trainable parameters. Although we did not compute entanglement entropy explicitly, this layout is known to generate strong bipartite and multipartite entanglement in shallow hardware-efficient circuits [83, 11, 79].

Compared to the QNN models discussed above, we can see that the classical feed-forward neural networks (NNs) exhibit a more flexible scaling pattern, with trainable parameters scale as  $\mathcal{O}(h_i h_{i+1})$ , where  $h_i$  and  $h_{i+1}$  denote the number of neurons in two consecutive layers  $l_i$  and  $l_{i+1}$  with independent selection of the neurons. As a result, while classical models depend on deep architectures and larger parameter counts, quantum networks achieve expressivity by utilizing intrinsic quantum correlations and exponential scaling of the Hilbert space. Consequently, incorporating a QNN between two consecutive classical layers, like the structure shown Fig. 1, with number of qubits much less than the number of neurons can reduce the number of parameters from, say,  $\mathcal{O}(h_i h_{i+1})$  to  $\mathcal{O}(h_i n_i + q_{\text{params}} + n_i h_{i+1})$  where  $n_i$  is the number of qubits and  $q_{\text{params}}$  represents the quantum circuit parameters.

## 5 Implementation and Training

### 5.1 CV-Circuit QCPINN

We implemented the preprocessor and the postprocessor (as in Fig. 1) with one hidden layer with 50 neurons and Tanh activation function. We used the PennyLane framework [63] with the Strawberry Fields Fock backend [86] for the CV-Circuit QCPINN implementation. Each CV-Circuit layer was configured for two qumodes with a cutoff dimension of 20. Quantum parameters were initialized using controlled random distributions, with small values for active parameters (e.g.,  $r$ ,  $d$ ) to ensure numerical stability. Classical neural network layers were initialized using Xavier initialization [87]. During training, either position quadrature (X) or number operator expectation measurements are performed on each qumode to extract continuous-valued features from the quantum state.

As CV-circuits rely on continuous degrees of freedom, their operations are inherently more sensitive to parameter scaling than those in DV systems. This sensitivity often manifests as instability during training, particularly when parameters grow large or when nonlinear transformations amplify fluctuations in the quantum state. For instance, squeezing operations are highly sensitive to large values, as excessive squeezing amplifies quadrature fluctuations, which increase photon number variance and truncation errors in Fock-space representations [88]. Similarly, displacement operations are constrained to prevent quantum states from exceeding computational cutoffs, as this can introduce simulation errors [89]. Likewise, the nonlinear operations such as the Kerr gate can cause phase shifts that scale quadratically with photon numbers, making them highly sensitive to large values [90].

Therefore, we used a learning rate of  $1.0 \times 10^{-4}$  to address the model’s sensitivity to gradient updates. A ReduceLROnPlateau scheduler was implemented with a patience of 20 epochs, decreasing the learning rate by a factor of 0.5

when no improvement was observed, down to a minimum of  $1.0 \times 10^{-6}$ . Additionally, we applied gradient clipping to prevent exploding gradients, restricting their norm to a maximum of 0.1. We also scaled the training parameters by small factors to further stabilize the CV transformations. While these settings can alleviate the instability and prevent divergence in quantum state evolution, they can also introduce the vanishing gradient problem [87].

## 5.2 DV-Circuit QCPINN

Similar to the CV-Circuit QCPINN, the preprocessor and the postprocessor consist of one hidden layer with 50 neurons and the Tanh activation function. We used Adam optimizer with a learning rate of 0.005 to train the DV-Circuit QCPINN. A learning rate scheduler, ReduceLRonPlateau, is employed to adjust the learning rate when the loss plateaus dynamically. Specifically, the scheduler reduces the learning rate by a factor of 0.9 if no improvement is observed for 1000 consecutive epochs, promoting stability and convergence. Furthermore, the training function applies gradient clipping to prevent exploding gradients, clipping them according to their norm to ensure they do not exceed a unity value. During training, Pauli-Z expectation measurements are performed on each qubit to extract features from the quantum state.

In all DV-Circuit QCPINN experiments, we set the number of shots to None to enable analytic gradient computation through backpropagation with PennyLane. This configuration activates the deterministic simulation mode, allowing continuous gradients to flow through the quantum circuit and enabling differentiation with backpropagation. Using a finite number of shots would introduce stochastic sampling noise, which would disrupt compatibility with backpropagation and require alternative differentiation methods, such as the parameter-shift rule, that are significantly more computationally expensive.

## 5.3 Classical PINN Models

The baseline PINN models consist of three main components: a preprocessing network, a neural network NN, and a postprocessing network (as shown in Fig. 1). The preprocessor and the postprocessor contain one hidden layer with 50 neurons and the Tanh activation function. The NN has two different configurations:

1. Model-1 includes two fully connected layers, each containing 50 neurons with a Tanh activation function between layers, and
2. Model-2 retains only the preprocessing and postprocessing networks, entirely omitting the NN to simplify the model’s structure.

These two models represent different levels of complexity, with model-1 having more layers and, consequently, a higher number of trainable parameters than model-2. We use these baseline PINN models to evaluate and compare the performance of the proposed hybrid models in Fig 1.

## 5.4 PDEs

We implemented five distinct PDEs, which include the Helmholtz, the time-dependent 2D lid-driven Cavity, the 1D Wave, the Klein-Gordon, and a Convection-diffusion problem. The mathematical formulation, boundary conditions, and corresponding loss function designs for each PDE are detailed in A.

## 5.5 Experiment Setup

We used PyTorch’s automatic differentiation to compute the gradients for both classical and quantum parameters, and the Adam optimizer. The training was carried out with a batch size of 64 and a maximum of 20,000 epochs. For the Cavity problem, the entire training dataset was generated using the Sobol sequence; in other cases, random sampling was sufficient throughout the training process. Training settings, including the optimizer and batch size, were kept consistent in QCPINN models to allow for a fair comparison with the baseline PINN. While altering configurations, such as increasing iterations or adjusting the batch size, might improve performance, the aim is to evaluate the models under identical conditions. Given the near-infinite hyperparameter space, this controlled evaluation ensures a fair assessment of the relative strengths and limitations of each approach.

In our initial implementation, we observed that the experiments on the CPU were faster than those on the GPU. This is likely due to our study’s relatively small batch size, circuit complexity, and limited number of qubits/qumodes: five qubits for DV-Circuit models and two qumodes for CV-based models. Moreover, the quantum backends employed in our experiments are not fully optimized for GPU efficiency. Considering these limitations, we have conducted our experiments on a CPU system with 6148 CPUs (each operating at 2.40 GHz) and 192 GB of RAM.

Table 3: Comparing the results of the best configuration of DV-Circuit QCPINN with PINN. Reported metrics include  $N_p$ : the number of trainable parameters;  $L_2$ : relative error (in %), and the mean  $\pm$  std across 10 independent runs;  $L_{\text{final}}$ : final loss; T: time per iteration (in sec), M: peak memory consumption (in MB). For the Cavity problem,  $u$  and  $v$ : velocity and  $p$ : pressure, and for other cases,  $u$ : reference solution and  $f$ : source term. For results with additional configurations, see Table 5, 6 and 7 in the appendix.

PDEs	Model		$N_p$		$L_2$	$\mathcal{L}_{\text{final}}$	T	M
Helmholtz Eq. 5	QCPINN	Angle-Cascade	771	$u$	$6.69 \pm 1.51$	$4.52 \pm 1.86$	$0.17 \pm 0.01$	$420.0 \pm 0.0$
				$f$	$2.86 \pm 0.54$			
	PINN	Model-2	2751	$u$	$12.12 \pm 7.17$	$5.04 \pm 3.12$	$0.002 \pm 0.01$	$340.0 \pm 0.0$
				$f$	$3.23 \pm 1.19$			
Cavity Eq. 6	QCPINN	Angle-Cascade	923	$u$	$25.73 \pm 2.49$	$0.10 \pm 0.02$	$0.36 \pm 0.01$	$540.0 \pm 0.0$
				$v$	$38.00 \pm 3.76$			
				$p$	$42.65 \pm 8.69$			
	PINN	Model-1	8003	$u$	$21.61 \pm 6.68$	$0.06 \pm 0.02$	$0.01 \pm 0.0$	$440.0 \pm 0.0$
				$v$	$34.24 \pm 2.76$			
				$p$	$34.82 \pm 5.25$			
Wave Eq. 7	QCPINN	Angle-Cross-mesh	796	$u$	$12.44 \pm 4.42$	$0.09 \pm 0.03$	$0.38 \pm 0.08$	$469.0 \pm 0.0$
	PINN	Model-2	2751	$u$	$11.13 \pm 1.78$	$0.05 \pm 0.01$	$0.02 \pm 0.02$	$351 \pm 0.00$
Klein-Gordon Eq. 8	QCPINN	Angle-Cascade	771	$u$	$4.24 \pm 1.88$	$0.27 \pm 0.10$	$0.25 \pm 0.03$	$447.0 \pm 0.0$
				$f$	$1.72 \pm 0.50$			
	PINN	Model-2	2751	$u$	$4.48 \pm 1.72$	$0.34 \pm 0.13$	$0.02 \pm 0.02$	$350.0 \pm 0.0$
				$f$	$1.79 \pm 0.47$			
Convection-diffusion Eq. 9	QCPINN	Angle-Cross-mesh	821	$u$	$4.54 \pm 2.17$	$0.001 \pm 0.001$	$0.42 \pm 0.11$	$468.0 \pm 0.0$
				$f$	$2.63 \pm 1.61$			
	PINN	Model-1	7901	$u$	$12.62 \pm 6.05$	$0.02 \pm 0.02$	$0.01 \pm 0.0$	$348.0 \pm 0.0$
				$f$	$5.57 \pm 3.05$			

## 6 Results

We first investigated the performance of the CV-Circuit QCPINN models across twelve distinct configurations, encompassing two measurement schemes, three nonlinear operations, and two parameterization strategies (as summarized in Table 1). These configurations were evaluated on the Helmholtz and lid-driven Cavity problems to assess their stability and convergence characteristics. However, the training behavior of the CV-Circuit models was found to be highly unstable, regardless of the configuration tested. Results are discussed in B in detail. In particular, Table 4 and Fig. 9 report the corresponding solution accuracy and training convergence for two representative configurations.

Following the CV-Circuit analysis, we systematically evaluated the DV-Circuit QCPINN models across a set of configurations comprising two embedding schemes and four circuit topologies. These quantum architectures were benchmarked against baseline PINN models discussed in 5.3 to assess their relative performance in terms of accuracy, convergence, parameter efficiency, time, and memory. We report the results of the best-performing configurations, while the complete set of results for all DV-Circuit configurations is provided in Appendix C for reference.

### 6.1 Helmholtz Equation

Table 3 presents the performance of the best-performing DV-Circuit QCPINN for solving the Helmholtz equation 5 and comparing the results with the best-performing PINN. The QCPINN (Angle-Cascade) with 771 parameters outperforms the PINN (Model-2) with 2751 parameters, achieving a parameter reduction of  $\sim 72\%$ . This results in a  $\sim 45\%$  lower relative  $L_2$  error for the solution field  $u$  (6.69% vs 12.12%) and 11% lower error for the force term  $f$  (2.86% vs 3.23%) at the expense of time and memory.

Fig. 3 compares the training loss history of the best-performing models. The curve shows the mean loss over ten independent runs, with shaded regions indicating the standard deviation. Both models exhibit stable convergence, with the QCPINN achieving slightly lower final loss and reduced variance, indicating more consistent training performance across runs despite using significantly fewer trainable parameters.

Fig. 4 presents the reference and predicted solutions, along with the corresponding absolute error distributions. Both QCPINN and PINN models accurately capture the overall solution pattern with visible deviations near the domain boundaries and regions with sharp local gradients.

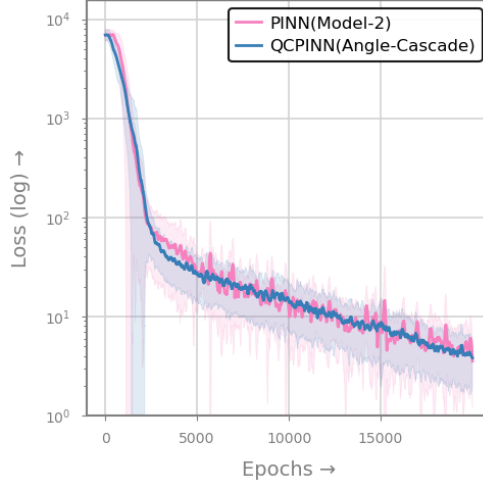


Figure 3: Comparison of the loss history of the best models of DV-Circuit QCPINN (Angle-Cascade) with PINN (Model-2) for solving the Helmholtz equation. For loss history of additional models, see Fig. 10 in the appendix.

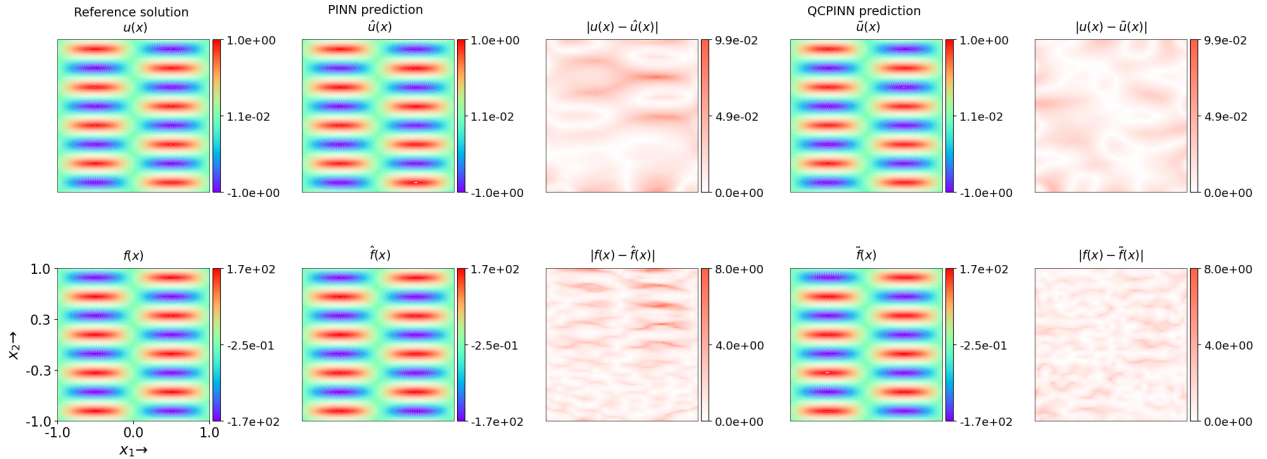


Figure 4: Comparison between the reference solution and model predictions for the Helmholtz equation. This includes the best results from our DV-Circuit QCPINN (Angle-Cascade) alongside PINN (Model-2). The first row shows the PDE solution  $u$ , while the second row shows the force field  $f$ .

## 6.2 Time-dependent 2D Lid-driven Cavity Equation

Table 3 shows that the lid-driven Cavity problem presents a balanced trade-off between parameter efficiency and predictive accuracy. The QCPINN (Angle-Cascade) achieves an  $\sim 88\%$  reduction in trainable parameters compared to PINN Model-1 (923 vs 8003), demonstrating substantial model compactness. Although this reduction is accompanied by modest increases in the relative errors for the velocity components  $u$ ,  $v$ , and  $p$  ( $\sim 19\%$ ,  $\sim 11\%$ , and  $\sim 23\%$ , respectively).

Fig. 5 compares the training loss convergence. Both models achieve stable convergence with minimal oscillations, indicating well-behaved optimization. The QCPINN reaches a slightly higher final loss value (0.10 vs 0.06) as shown in Table 3 but follows a smoother convergence trajectory, suggesting stable learning dynamics even with significantly fewer parameters.

Fig. 6 visualizes the predicted velocity and pressure fields along with their absolute error maps. Both models reproduce the dominant flow structure, including the central primary vortex and secondary corner eddies, indicating that they effectively capture the overall flow dynamics. However, significant differences emerge in the pressure field. The largest pressure errors for both models occur near the upper moving lid and corner regions, where sharp velocity gradients and strong shear layers lead to steep pressure variations. These regions are inherently challenging for PINN-based

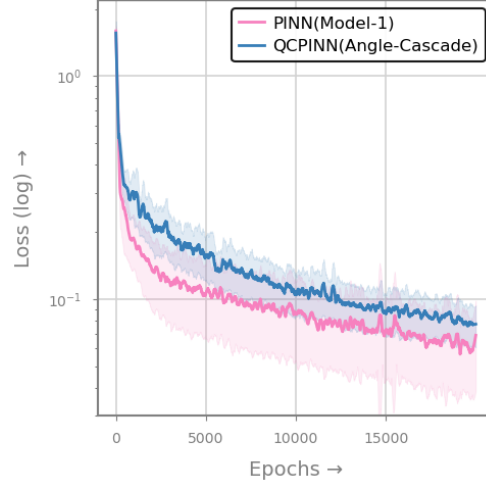


Figure 5: Training loss history for the Cavity problem. The plots compare the convergence behavior of the QCPINN (Angle-Cascade) model with the best-performing PINN (Model-1).

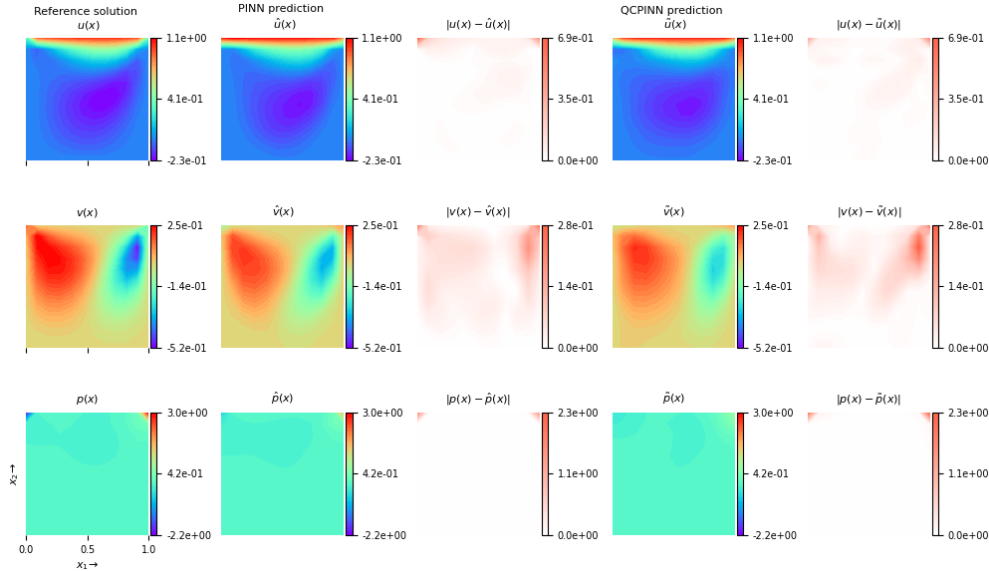


Figure 6: Comparison of the reference FEM solution and the model predictions for the lid-driven Cavity problem: the PINN Model-1, and QCPINN (Angle-Cascade). The first and second rows show the velocity fields ( $u$  and  $v$ ), while the third row shows the pressure field ( $p$ ).

models, as the physics-informed loss involves higher-order derivatives that amplify numerical sensitivity in zones with discontinuous boundary forcing.

### 6.3 Additional PDEs

Results from all three additional PDEs (Wave, Klein-Gordon, and Convection-diffusion) consistently show that Angle embedding significantly outperforms Amplitude embedding across all examined cases. Additionally, the Cascade and Cross-mesh topologies demonstrated superior performance compared to the other topologies tested. Building on these findings, we conducted further tests on these PDEs using the most effective configurations. The results are presented in Table 3, while additional results can be found in Table 7 in the appendix.

For the Wave equation, the Angle-Cross-mesh QCPINN attains a  $\sim 71.1\%$  reduction in parameters (796 vs. 2751) with a slightly higher,  $\sim 11.8\%$  increase, in relative  $L_2$  error for  $u$  (12.44% vs. 11.13%).

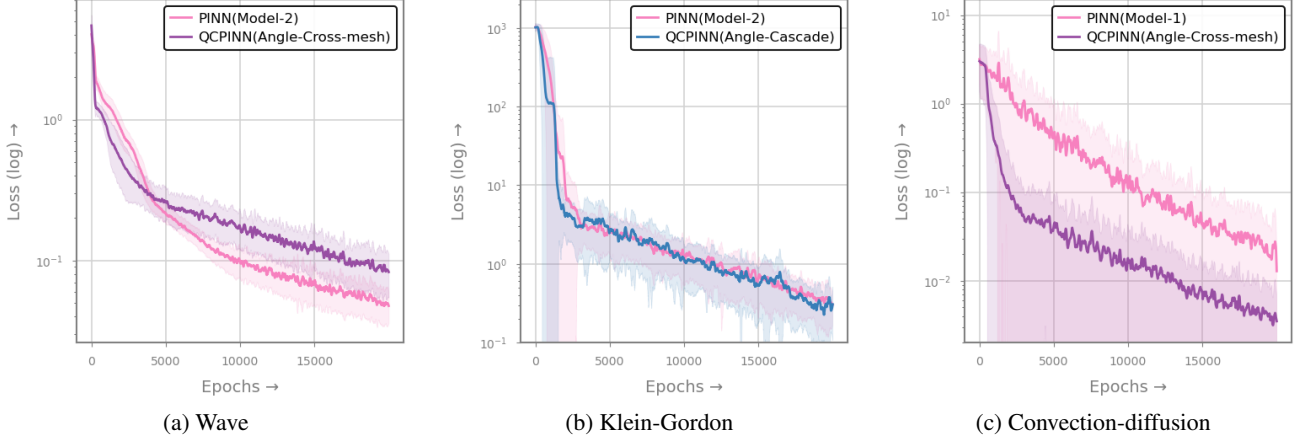


Figure 7: Training loss history for additional PDEs. Each plot compares the convergence behavior of the best QCPINN model against the best-performing PINN model.

For the Klein-Gordon equation, the Angle-Cascade QCPINN yields  $\sim 72.0\%$  parameter savings (771 vs. 2751) while slightly improving accuracy: the mean  $L_2$  error for  $u$  decreases from 4.48% to 4.24%,  $\sim 5.4\%$  relative improvement, and the error for  $f$  decreases marginally,  $\sim 3.9\%$ . These differences are small and lie within the reported standard deviations, indicating comparable performance with fewer parameters.

In Convection-diffusion equation, the Angle-Cascade QCPINN demonstrates both large parameter efficiency (821 vs. 7901 parameters,  $\sim 89.6\%$  reduction) and substantially better accuracy: the mean  $L_2$  error for  $u$  falls from 12.62% to 4.54% ( $\sim 64.0\%$  relative improvement), and the error for  $f$  decreases from 5.57% to 2.63% ( $\sim 52.8\%$  relative improvement). As shown in Table 7, all QCPINN models perform well on this problem. This case shows a clear advantage of the QCPINN architecture in capturing sharp localized features typical of convection-dominated flows.

Fig. 7 compares the training loss histories of these models across the additional PDEs. For the Wave equation, Fig. 7(a) shows that the QCPINN achieves faster initial convergence, reaching lower loss values within the first 4,000 epochs before the baseline PINN (Model-2) begins to converge more rapidly in the later stages.

For the Klein-Gordon equation, Fig. 7(b) demonstrates that both models follow nearly similar convergence trajectories. In contrast, for the Convection-diffusion equation, Fig. 7(c) highlights a clear advantage for the QCPINN, which exhibits a steadily decreasing loss throughout training and attains a final loss approximately an order of magnitude lower than the classical model. This result aligns with Table 3, where the QCPINN achieved lower relative  $L_2$  errors, confirming its better capability in handling convection-dominated dynamics with sharp localized gradients.

## 6.4 Memory and Time Consideration

Across all experiments, the QCPINN models demonstrate a significant increase in computational time per iteration, exhibiting a 15 to 40-fold increase compared to PINN approaches. This discrepancy highlights the computational overhead associated with simulating quantum circuits on classical hardware. The memory consumption remains relatively consistent between quantum and classical approaches, ranging from 420 to 540 MB for QCPINN models, compared to 340 to 440 MB for conventional PINN models. This observation suggests that the hybrid architecture does not impose additional memory requirements. While the computational overhead is a characteristic of the simulator, we anticipate that substantial advantages will become evident as quantum hardware becomes more accessible and practical for implementation.

## 7 Discussion

**Circuit Topology and Entanglement in QCPINN.** Both the Cross-mesh and Cascade topologies share key structural properties that contribute to their good performance in the QCPINN models. Each employs parameterized controlled-rotation (CRX or CRZ) gates that introduce continuously tunable entanglement between qubits, supporting smoother

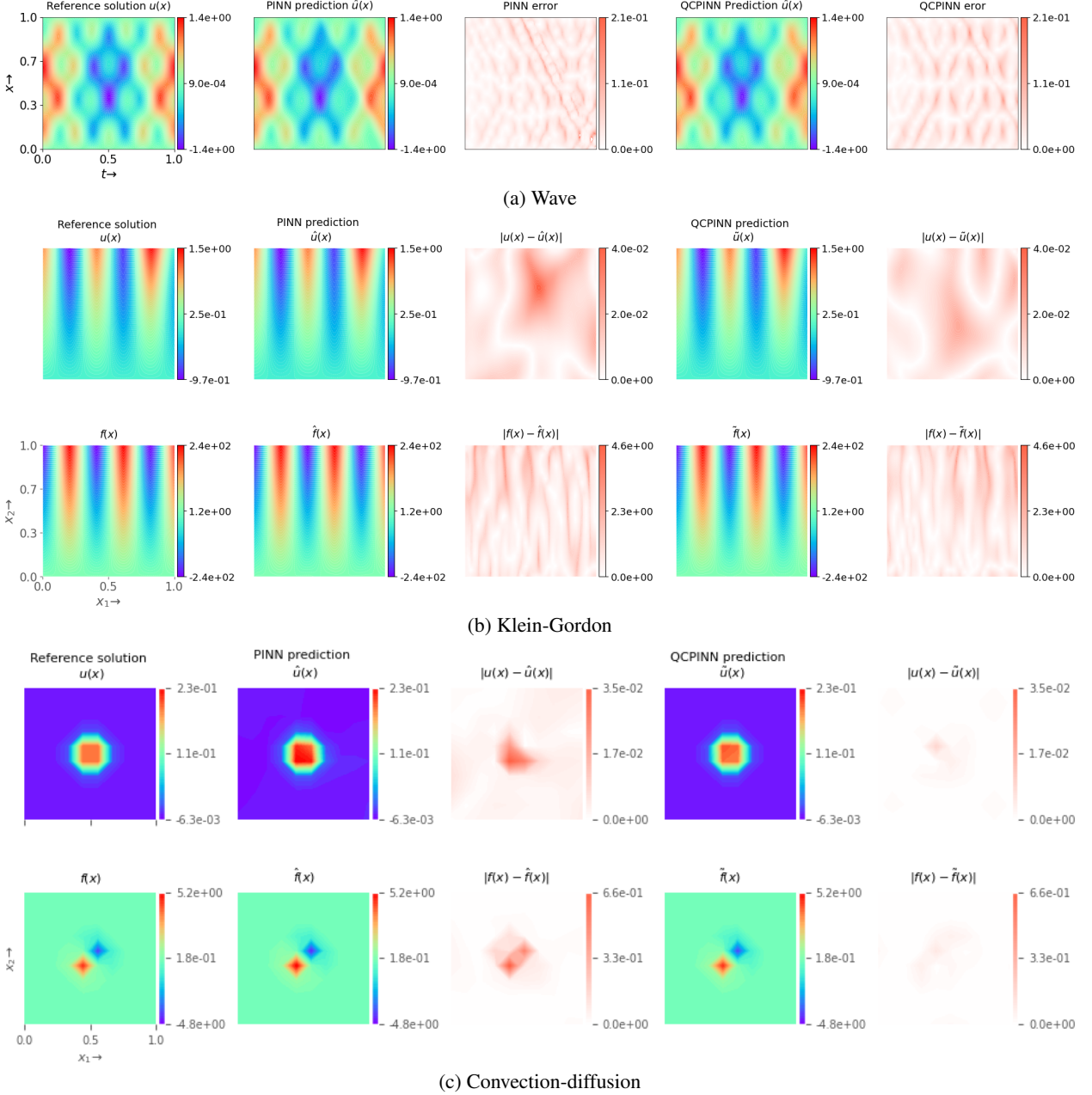


Figure 8: Comparison of the reference solution and the model predictions for additional PDEs. For each equation, we present results from both the best-performing PINN and DV-Circuit QCPINN models. For each equation, the top row displays the velocity field ( $u$ ), while the bottom row (if it exists) shows the force field ( $f$ ).

gradient propagation and mitigating barren-plateau effects during hybrid training (as in Table 5, 6, and 7, and Fig. 10, 11, and 12). While the Cascade design distributes entanglement efficiently through a ring topology at shallow depth, the Cross-mesh circuit extends this advantage to an all-to-all connectivity pattern. In contrast, the Alternate and Layered circuits rely on fixed CNOT gates, generating discrete, local entangling operations that offer limited tunability and are more prone to optimization plateaus, as reflected in their slower convergence and higher residual losses for the Wave equation (as in Table 7 and Fig. 12(a)).

Overall, the comparison indicates that hybrid QCPINN architectures benefit most from hardware-efficient ansätze with continuous entanglement control, such as the Angle-Cascade and Angle-Cross-mesh circuits. These configurations

offer a favorable balance between expressivity, trainability, and hardware feasibility, making them highly suitable for near-term quantum solvers of PDEs.

**Angle vs. Amplitude Embedding.** Results consistently demonstrate that Angle embedding achieves better performance compared to Amplitude embedding across all tested configurations (as in Table 5 and 6). This advantage arises from both theoretical and practical considerations. First, Amplitude embedding represents the data as quantum state amplitudes that must satisfy the normalization constraint  $\sum_i |a_i|^2 = 1$ , coupling all input features globally and introducing nonlinear dependencies that complicate optimization. Second, it scales poorly with input dimensionality, requiring  $2^n$  amplitudes to encode  $n$  features, which often require zero-padding (or, in our case, we can also use a classical preprocessor with  $2^n$  outputs, which increases expressivity by introducing new trainable parameters but does not yield better results, probably due to global coupling through normalization constraint and degraded gradient flow during backpropagation).

In contrast, Angle embedding directly maps each classical feature to a rotation angle on a single qubit through parameterized gates such as  $RX(\theta)$ , allowing local and differentiable embeddings with straightforward gradient computation via automatic differentiation. Hence, it provides hardware-efficient, normalization-free feature mapping in which each input independently controls one qubit rotation, yielding stable gradients, better generalization, and faster convergence. Empirically, our angle-encoded circuits (e.g., Angle-Cascade) achieved 45–64% lower relative  $L_2$  errors than their amplitude-encoded counterparts across the Helmholtz and Cavity problems (as in Table 5 and 6), confirming that feature-to-rotation mappings are better suited for such hybrid QCPINN architectures.

**Feasibility and Noise Analysis.** While all experiments in this study were performed on noise-free simulators, practical implementations on near-term quantum processors will inevitably be affected by shot noise from finite measurements, gate infidelity, and decoherence ( $T_1/T_2$  relaxation). Nevertheless, the feasibility of implementing the proposed QCPINN models on near-term quantum hardware depends on qubit or qumode requirements, circuit depth, entanglement cost, sampling demands, and expected resilience to device noise.

For the DV-Circuit QCPINN, the most effective configurations were the Angle-Cascade and Angle-Cross-mesh topologies. Both were implemented with five qubits and a single quantum layer ( $L = 1$ ), as summarized in section 5. The circuit depth and entangling gate counts vary by topology, as detailed in Table 2:

- The Angle–Cascade circuit follows a ring topology with moderate expressivity and hardware efficiency. Its circuit depth scales as  $(n + 2)L = 7$ , using about five entangling gates and roughly 15 trainable parameters. This shallow depth and limited entanglement make it well-suited for current NISQ devices, which typically tolerate 10-20 two-qubit gates before decoherence significantly impacts fidelity [59].
- The Angle–Cross-mesh circuit adopts all-to-all qubit connectivity. Its depth scales as  $(n^2 - n + 4)L = 24$  for  $n = 5$ , with approximately 20 entangling gates and 45 trainable parameters. Despite being deeper, this layout remained tractable.

For hardware-based training, gradient estimation generally requires 2000–5000 shots per iteration to maintain sampling error below 1% in observable expectations [11]. Dominant hardware noise sources include gate infidelity, readout errors, and  $T_1/T_2$  relaxation. The state-of-the-art superconducting quantum processors achieve single-qubit gate fidelities of 99.9% [91, 92] and two-qubit fidelities around 99.3-99.7% [93, 94]. Thus, a depth-24 circuit retains effective end-to-end fidelity exceeding 90% before readout correction.

**Hyperparameter Sensitivity of CV-Circuit QCPINN Models.** Although the CV-Circuit QCPINN models did not achieve the same performance levels as their DV-based counterparts, these results remain significant for understanding the current feasibility limits of CV quantum neural networks in physics-informed learning. The observed training failures primarily arose from vanishing gradients imposed by stability constraints, compounded by the intrinsic challenges of PINN optimization, namely, high-order differential requirements and a highly non-convex residual loss landscape. These factors intensified the barren plateau effect, leading to persistent residual loss oscillations with minimal improvement over thousands of iterations (Fig. 9). In other words, the conflict between maintaining valid quantum states (favoring small parameter initialization) and achieving sufficient gradient magnitudes restricted trainability. Among all hyperparameters, the cutoff dimension, learning rate, and initialization scale of active gates (squeezing and displacement amplitudes) exerted the greatest influence on whether training could escape these plateaus.

Importantly, the fact that the measurement scheme and nonlinearity choice (as in Table 1) had minimal impact on performance suggests that the bottleneck lies not in CV-Circuit expressivity, which remains theoretically superior due to their infinite-dimensional Hilbert spaces, but in the optimization landscape dominated by barren plateaus and restricted gradient flow. This insight directs future research toward developing optimization strategies specifically designed to mitigate barren plateaus in continuous-variable systems (e.g., natural-gradient descent, adaptive parameter-shift rules, layer-wise training, or gradient-free evolutionary methods) rather than further modifying circuit architectures.

**Limitations and Future Work.** Although parameter efficiency was significantly improved, overall solution accuracy remained comparable to baseline PINNs, especially for Cavity and Wave equations, where there is still room for enhancement. Additionally, the highly non-convex PINN loss landscape still required careful weighting for the loss terms, which were determined through extensive empirical studies rather than exploring quantum circuit advantage to address this challenge. Contrary to theoretical expectations, CV-Circuit implementations exhibited training instabilities and underperformed relative to DV-Circuit variants for the cases considered in this study. Looking ahead, the promise of quantum-enhanced PINNs in practical applications is evident. Future work should include validation of QCPINN models on quantum hardware to evaluate their resilience to noise and sampling errors— both critical for real-world applications. Additionally, developing advanced quantum circuit designs tailored to PDEs and optimizing training stability, especially for CV methods, will further advance the integration of quantum computing and machine learning for solving complex problems across diverse fields.

## 8 Conclusion

We found that QCPINN models achieve comparable solution accuracy to baseline PINNs while requiring a fraction of trainable parameters, as little as 10-30% of those needed by their classical counterparts under about the same settings. The experimental evidence supports our hypothesis that hybrid quantum-classical approaches can maintain solution quality while dramatically improving parameter efficiency. Our systematic assessment of various QCPINN configurations across multiple PDEs consistently revealed that DV-Circuit implementations with Angle embedding and either Cascade or Cross-mesh topologies offer the best performance. Angle embedding is superior to Amplitude embedding due to its simplicity and gradient stability, as it maps data to individual qubit rotations without normalization constraints, allowing for stable backpropagation. The Cascade topology balances expressivity and efficiency, providing enough entanglement to capture complex PDE relationships while keeping circuit depth manageable and avoiding barren plateaus. The Cross-mesh topology, on the other hand, leverages all-to-all qubit connectivity to enhance the circuit’s expressivity and its ability to represent globally correlated solution features across the spatial domain of PDEs. While this design increases the number of entangling gates and circuit depth relative to the Cascade layout, our experiments show that the added expressivity improves generalization and convergence stability without excessive parameter growth. For the Helmholtz, Klein-Gordon, and Convection-diffusion equations, our QCPINN achieved a significant reduction of around 4–64% in relative  $L_2$  error across various fields compared to baseline PINN models. In contrast, for the Cavity and Wave equations, the  $L_2$  error was slightly higher across various fields compared to the baseline PINN models. CV-Circuits exhibit persistent training instabilities as standard gradient-based optimization methods, such as Adam, face significant challenges with CV-based quantum circuit models due to their sensitivity to parameter initialization and gradient dynamics. The findings in this study can be used as a practical guideline for designing hybrid quantum–classical neural architectures to solve PDEs with improved parameter efficiency and stable convergence. The open-source implementation further enhances reproducibility and enables community engagement.

## Acknowledgment

We thank the National Center for High-Performance Computing of Turkiye (UHem) for providing computing resources under grant number 5010662021.

**Keywords** Quantum Computing · Neural networks · Physics-informed neural network · Partial differential equation · PINN · PDE

## References

- [1] George Em Karniadakis, Ioannis G Kevrekidis, Lu Lu, Paris Perdikaris, Sifan Wang, and Liu Yang. Physics-informed machine learning. *Nature Reviews Physics*, 3(6):422–440, 2021.
- [2] Shengze Cai, Zhiping Mao, Zhicheng Wang, Minglang Yin, and George Em Karniadakis. Physics-informed neural networks (PINNs) for fluid mechanics: a review. *Acta Mechanica Sinica*, 37(12):1727–1738, 2021.
- [3] Afrah Farea, Saiful Khan, Reza Daryani, Emre Cenk Ersan, and Mustafa Serdar Celebi. Learning Fluid-Structure Interaction Dynamics with Physics-Informed Neural Networks and Immersed Boundary Methods. *arXiv preprint arXiv:2505.18565*, 2025.
- [4] Afrah Farea, Saiful Khan, and Mustafa Serdar Celebi. Multi-Objective Loss Balancing in Physics-Informed Neural Networks for Fluid Flow Applications. In *32nd IEEE Int. Conf. on High Performance Computing, Data, and Analytics (accepted)*, 2025.

- [5] Zheyuan Hu, Khemraj Shukla, George Em Karniadakis, and Kenji Kawaguchi. Tackling the curse of dimensionality with physics-informed neural networks. *Neural Networks*, 176:106369, 2024.
- [6] Zheyuan Hu, Zhouhao Yang, Yezhen Wang, George E Karniadakis, and Kenji Kawaguchi. Bias-Variance Trade-Off in Physics-Informed Neural Networks with Randomized Smoothing for High-Dimensional PDEs. *SIAM Journal on Scientific Computing*, 47(4):C846–C872, 2025.
- [7] Xue Ying. An Overview of Overfitting and its Solutions. *Journal of Physics: Conf. Series*, 1168(2):022022, 2019.
- [8] Afrah Farea and Mustafa Serdar Celebi. Learnable activation functions in physics-informed neural networks for solving partial differential equations, 2025.
- [9] Kosuke Mitarai, Makoto Negoro, Masahiro Kitagawa, and Keisuke Fujii. Quantum circuit learning. *Physical Review A*, 98(3):032309, 2018.
- [10] Vojtěch Havlíček, Antonio D Córcoles, Kristan Temme, Aram W Harrow, Abhinav Kandala, Jerry M Chow, and Jay M Gambetta. Supervised learning with quantum-enhanced feature spaces. *Nature*, 567(7747):209–212, 2019.
- [11] Marco Cerezo, Andrew Arrasmith, Ryan Babbush, Simon C Benjamin, Suguru Endo, Keisuke Fujii, Jarrod R McClean, Kosuke Mitarai, Xiao Yuan, Lukasz Cincio, et al. Variational quantum algorithms. *Nature Reviews Physics*, 3(9):625–644, 2021.
- [12] Martin Knudsen and Christian B. Mendl. Solving Differential Equations via Continuous-Variable Quantum Computers. *arXiv preprint arXiv:2206.14184*, 2020.
- [13] Maria Schuld, Ryan Sweke, and Johannes Jakob Meyer. Effect of data encoding on the expressive power of variational quantum-machine-learning models. *Physical Review A*, 103(3):032430, 2021.
- [14] Amira Abbas, David Sutter, Christa Zoufal, Aurélien Lucchi, Alessio Figalli, and Stefan Woerner. The power of quantum neural networks. *Nature Computational Science*, 1(6):403–409, 2021.
- [15] Yuxuan Du, Min-Hsiu Hsieh, Tongliang Liu, Shan You, and Dacheng Tao. Learnability of Quantum Neural Networks. *PRX quantum*, 2(4):040337, 2021.
- [16] Alexandr Sedykh, Maninadh Podapaka, Asel Saginalieva, Karan Pinto, Markus Pflitsch, and Alexey Melnikov. Hybrid quantum physics-informed neural networks for simulating computational fluid dynamics in complex shapes. *Machine Learning: Science and Technology*, 5(2):025045, 2024.
- [17] Nahid Binandeh Dehaghani, A Pedro Aguiar, and Rafal Wisniewski. A Hybrid Quantum-Classical Physics-Informed Neural Network Architecture for Solving Quantum Optimal Control Problems. In *2024 IEEE Int. Conf. on Quantum Computing and Engineering (QCE)*, volume 1, pages 1378–1386. IEEE, 2024.
- [18] Corey Trahan, Mark Loveland, and Samuel Dent. Quantum Physics-Informed Neural Networks. *Entropy*, 26(8):649, 2024.
- [19] Fong Yew Leong, Wei-Bin Ewe, Si Bui Quang Tran, Zhongyuan Zhang, and Jun Yong Khoo. Hybrid quantum physics-informed neural network: Towards efficient learning of high-speed flows. *Computers & Fluids*, page 106782, 2025.
- [20] Afrah Farea. QCPINN: Quantum Classical Physics-Informed Neural Networks for Solving PDEs. <https://github.com/afrah/QCPINN>, 2025. Accessed: 2025-10-13.
- [21] Aram W Harrow, Avinandan Hassidim, and Seth Lloyd. Quantum Algorithm for Linear Systems of Equations. *Physical Review Letters*, 103(15):150502, 2009.
- [22] Andris Ambainis. Variable time amplitude amplification and quantum algorithms for linear algebra problems. In Thomas Wilke Christoph Dürr, editor, *Symposium on Theoretical Aspects of Computer Science*, volume 14, pages 636–647, Paris, France, 2012.
- [23] Rolando Somma, Andrew Childs, and Robin Kothari. Quantum linear systems algorithm with exponentially improved dependence on precision. In *APS March Meeting Abstracts*, volume 2016, pages H44–001. APS, 2016.
- [24] Sarah K Leyton and Tobias J Osborne. A quantum algorithm to solve nonlinear differential equations. *arXiv preprint arXiv:0812.4423*, 2008.
- [25] Dominic W Berry. High-order quantum algorithm for solving linear differential equations. *Journal of Physics A: Mathematical and Theoretical*, 47(10):105301, 2014.
- [26] Andrew M Childs and Jin-Peng Liu. Quantum Spectral Methods for Differential Equations. *Communications in Mathematical Physics*, 375(2):1427–1457, 2020.
- [27] Dominic W Berry, Andrew M Childs, Aaron Ostrander, and Guoming Wang. Quantum Algorithm for Linear Differential Equations with Exponentially Improved Dependence on Precision. *Communications in Mathematical Physics*, 356:1057–1081, 2017.

- [28] Jeffrey Yepez. Quantum Lattice-Gas Model for the Burgers Equation. *Journal of Statistical Physics*, 107:203–224, 2002.
- [29] Ashley Montanaro and Sam Pallister. Quantum algorithms and the finite element method. *Physical Review A*, 93(3):032324, 2016.
- [30] Furkan Oz, Rohit KSS Vuppala, Kursat Kara, and Frank Gaitan. Solving Burgers’ equation with quantum computing. *Quantum Information Processing*, 21(1):30, 2022.
- [31] Furkan Oz, Omer San, and Kursat Kara. An efficient quantum partial differential equation solver with chebyshev points. *Scientific Reports*, 13(1):7767, 2023.
- [32] John Preskill. Reliable quantum computers. *Proc. of the Royal Society of London. Series A: Mathematical, Physical and Engineering Sciences*, 454(1969):385–410, 1998.
- [33] Barbara M Terhal. Quantum error correction for quantum memories. *Reviews of Modern Physics*, 87(2):307–346, 2015.
- [34] Andrew M Childs, Yuan Su, Minh C Tran, Nathan Wiebe, and Shuchen Zhu. Theory of Trotter Error with Commutator Scaling. *Physical Review X*, 11(1):011020, 2021.
- [35] Sergey Bravyi and Alexei Kitaev. Universal quantum computation with ideal Clifford gates and noisy ancillas. *Physical Review A—Atomic, Molecular, and Optical Physics*, 71(2):022316, 2005.
- [36] Sergio Boixo, Sergei V Isakov, Vadim N Smelyanskiy, Ryan Babbush, Nan Ding, Zhang Jiang, Michael J Bremner, John M Martinis, and Hartmut Neven. Characterizing quantum supremacy in near-term devices. *Nature Physics*, 14(6):595–600, 2018.
- [37] Scott Aaronson. Read the fine print. *Nature Physics*, 11(4):291–293, 2015.
- [38] Carlo Ciliberto, Mark Herbster, Alessandro Davide Ialongo, Massimiliano Pontil, Andrea Rocchetto, Simone Severini, and Leonard Wossnig. Quantum machine learning: a classical perspective. *Proc. of the Royal Society A: Mathematical, Physical and Engineering Sciences*, 474(2209):20170551, 2018.
- [39] Seth Lloyd, Masoud Mohseni, and Patrick Rebentrost. Quantum algorithms for supervised and unsupervised machine learning. *arXiv preprint arXiv:1307.0411*, 2013.
- [40] Adrián Pérez-Salinas, David López-Núñez, Artur García-Sáez, P. Forn-Díaz, and José I. Latorre. One qubit as a universal approximant. *Physical Review A*, 104:012405, Jul 2021.
- [41] Takahiro Goto, Quoc Hoan Tran, and Kohei Nakajima. Universal Approximation Property of Quantum Machine Learning Models in Quantum-Enhanced Feature Spaces. *Physical Review Letters*, 127(9):090506, 2021.
- [42] Yunchao Liu, Srinivasan Arunachalam, and Kristan Temme. A rigorous and robust quantum speed-up in supervised machine learning. *Nature Physics*, 17(9):1013–1017, 2021.
- [43] Nathan Killoran, Thomas R Bromley, Juan Miguel Arrazola, Maria Schuld, Nicolás Quesada, and Seth Lloyd. Continuous-variable quantum neural networks. *Physical Review Research*, 1(3):033063, 2019.
- [44] Yudong Cao, Jonathan Romero, Jonathan P Olson, Matthias Degroote, Peter D Johnson, Mária Kieferová, Ian D Kivlichan, Tim Menke, Borja Peropadre, Nicolas PD Sawaya, et al. Quantum Chemistry in the Age of Quantum Computing. *Chemical reviews*, 119(19):10856–10915, 2019.
- [45] Bela Bauer, Sergey Bravyi, Mario Motta, and Garnet Kin-Lic Chan. Quantum Algorithms for Quantum Chemistry and Quantum Materials Science. *Chemical Reviews*, 120(22):12685–12717, 2020.
- [46] Benjamin Nachman, Davide Provasoli, Wibe A De Jong, and Christian W Bauer. Quantum Algorithm for High Energy Physics Simulations. *Physical Review Letters*, 126(6):062001, 2021.
- [47] Carlo A Trugenberger. Quantum Pattern Recognition. *Quantum Information Processing*, 1:471–493, 2002.
- [48] Alberto Peruzzo, Jarrod McClean, Peter Shadbolt, Man-Hong Yung, Xiao-Qi Zhou, Peter J Love, Alán Aspuru-Guzik, and Jeremy L O’Brien. A variational eigenvalue solver on a photonic quantum processor. *Nature communications*, 5(1):4213, 2014.
- [49] Jarrod R McClean, Jonathan Romero, Ryan Babbush, and Alán Aspuru-Guzik. The theory of variational hybrid quantum-classical algorithms. *New Journal of Physics*, 18(2):023023, 2016.
- [50] Carlos Bravo-Prieto, Ryan LaRose, Marco Cerezo, Yigit Subasi, Lukasz Cincio, and Patrick J Coles. Variational Quantum Linear Solver. *Quantum*, 7:1188, 2023.
- [51] Anton Simen Albino, Lucas Correia Jardim, Diego Campos Knupp, Antonio Jose Silva Neto, Otto Menegasso Pires, and Erick Giovani Sperandio Nascimento. Solving partial differential equations on near-term quantum computers. *arXiv preprint arXiv:2208.05805*, 2022.

- [52] Oleksandr Kyriienko, Annie E Paine, and Vincent E Elfving. Solving nonlinear differential equations with differentiable quantum circuits. *Physical Review A*, 103(5):052416, 2021.
- [53] Daniel Bultrini and Oriol Vendrell. Mixed quantum-classical dynamics for near-term quantum computers. *Communications Physics*, 6(1):328, 2023.
- [54] Annie E Paine, Vincent E Elfving, and Oleksandr Kyriienko. Quantum kernel methods for solving regression problems and differential equations. *Physical Review A*, 107(3):032428, 2023.
- [55] Michael Lubasch, Jaewoo Joo, Pierre Moinier, Martin Kiffner, and Dieter Jaksch. Variational quantum algorithms for nonlinear problems. *Physical Review A*, 101(1):010301, 2020.
- [56] Samuel L Braunstein and Peter Van Loock. Quantum information with continuous variables. *Reviews of Modern Physics*, 77(2):513–577, 2005.
- [57] Abhishek Setty, Rasul Abdusalamov, and Felix Motzoi. Self-adaptive physics-informed quantum machine learning for solving differential equations. *Machine Learning: Science and Technology*, 6(1):015002, 2025.
- [58] John Preskill. Quantum Computing in the NISQ era and beyond. *Quantum*, 2:79, 2018.
- [59] Kishor Bharti, Alba Cervera-Lierta, Thi Ha Kyaw, Tobias Haug, Sumner Alperin-Lea, Abhinav Anand, Matthias Degroote, Hermanni Heimonen, Jakob S Kottmann, Tim Menke, et al. Noisy intermediate-scale quantum algorithms. *Reviews of Modern Physics*, 94(1):015004, 2022.
- [60] Aditi Krishnapriyan, Amir Gholami, Shandian Zhe, Robert Kirby, and Michael W Mahoney. Characterizing possible failure modes in physics-informed neural networks. *Advances in Neural Information Processing Systems*, 34:26548–26560, 2021.
- [61] J. Rishi, Azhar Gafoor, Sumanth Kumar, and Deepak Subramani. On the Training Efficiency of Shallow Architectures for Physics Informed Neural Networks. In *Computational Science – ICCS 2024*, volume 14834 of *Lecture Notes in Computer Science*, pages 363–377. Springer, 2024.
- [62] Yeonjong Shin, Zhongqiang Zhang, and George Em Karniadakis. Error estimates of residual minimization using neural networks for linear PDEs. *Journal of Machine Learning for Modeling and Computing*, 4(4), 2023.
- [63] Ville Bergholm, Josh Izaac, Maria Schuld, Christian Gogolin, Shahnawaz Ahmed, Vishnu Ajith, M Sohaib Alam, Guillermo Alonso-Linaje, B AkashNarayanan, Ali Asadi, et al. PennyLane: Automatic differentiation of hybrid quantum-classical computations. *arXiv preprint arXiv:1811.04968*, 2018.
- [64] Michael Broughton, Guillaume Verdon, Trevor McCourt, Antonio J Martinez, Jae Hyeon Yoo, Sergei V Isakov, Philip Massey, Ramin Halavati, Murphy Yuezheng Niu, Alexander Zlokapa, et al. TensorFlow Quantum: A Software Framework for Quantum Machine Learning. *arXiv preprint arXiv:2003.02989*, 2020.
- [65] Zongyi Li, Nikola Kovachki, Kamyar Aizzadenesheli, Burigede Liu, Kaushik Bhattacharya, Andrew Stuart, and Anima Anandkumar. Fourier Neural Operator for Parametric Partial Differential Equations. In *Int. Conf. on Learning Representations*, 2021.
- [66] Maziar Raissi, Paris Perdikaris, and George E Karniadakis. Physics-informed neural networks: A deep learning framework for solving forward and inverse problems involving nonlinear partial differential equations. *Journal of Computational Physics*, 378:686–707, 2019.
- [67] Sifan Wang, Yujun Teng, and Paris Perdikaris. Understanding and Mitigating Gradient Flow Pathologies in Physics-Informed Neural Networks. *SIAM Journal on Scientific Computing*, 43(5):A3055–A3081, 2021.
- [68] Sai Karthikeya Vemuri and Joachim Denzler. Gradient Statistics-Based Multi-Objective Optimization in Physics-Informed Neural Networks. *Sensors*, 23(21):8665, 2023.
- [69] Qiang Liu, Mengyu Chu, and Nils Thuerey. ConFIG: Towards Conflict-free Training of Physics Informed Neural Networks. In *The 13th Int. Conf. on Learning Representations*, 2024.
- [70] A. Ali Heydari, Craig A. Thompson, and Asif Mehmood. SoftAdapt: Techniques for Adaptive Loss Weighting of Neural Networks with Multi-Part Loss Functions. *CoRR*, abs/1912.12355, 2019.
- [71] Rafael Bischof and Michael A. Kraus. Multi-Objective Loss Balancing for Physics-Informed Deep Learning. *Computer Methods in Applied Mechanics and Engineering*, 439:117914, 2025.
- [72] Levi D McClenny and Ulisses M Braga-Neto. Self-adaptive physics-informed neural networks. *Journal of Computational Physics*, 474:111722, 2023.
- [73] Shirong Li and Xinlong Feng. Dynamic Weight Strategy of Physics-Informed Neural Networks for the 2D Navier–Stokes Equations. *Entropy*, 24(9):1254, 2022.
- [74] Francisco Sahli Costabal, Yibo Yang, Paris Perdikaris, Daniel E Hurtado, and Ellen Kuhl. Physics-Informed Neural Networks for Cardiac Activation Mapping. *Frontiers in Physics*, 8:42, 2020.

- [75] Pu Ren, Chengping Rao, Yang Liu, Jian-Xun Wang, and Hao Sun. PhyCRNet: Physics-informed convolutional-recurrent network for solving spatiotemporal PDEs. *Computer Methods in Applied Mechanics and Engineering*, 389:114399, 2022.
- [76] Ariel Norambuena, Marios Mattheakis, Francisco J González, and Raúl Coto. Physics-Informed Neural Networks for Quantum Control. *Physical Review Letters*, 132(1):010801, 2024.
- [77] Jarrod R McClean, Sergio Boixo, Vadim N Smelyanskiy, Ryan Babbush, and Hartmut Neven. Barren plateaus in quantum neural network training landscapes. *Nature communications*, 9(1):4812, 2018.
- [78] Marco Cerezo, Akira Sone, Tyler Volkoff, Lukasz Cincio, and Patrick J Coles. Cost function dependent barren plateaus in shallow parametrized quantum circuits. *Nature communications*, 12(1):1791, 2021.
- [79] Zoë Holmes, Kunal Sharma, Marco Cerezo, and Patrick J Coles. Connecting Ansatz Expressibility to Gradient Magnitudes and Barren Plateaus. *PRX quantum*, 3(1):010313, 2022.
- [80] Francesco Tacchino, Panagiotis Barkoutsos, Chiara Macchiavello, Ivano Tavernelli, Dario Gerace, and Daniele Bajoni. Quantum implementation of an artificial feed-forward neural network. *Quantum Science and Technology*, 5(4):044010, 2020.
- [81] Stefano Mangini, Francesco Tacchino, Dario Gerace, Daniele Bajoni, and Chiara Macchiavello. Quantum computing models for artificial neural networks. *Europhysics Letters*, 134(1):10002, 2021.
- [82] Edward Farhi and Hartmut Neven. Classification with Quantum Neural Networks on Near Term Processors. *arXiv preprint arXiv:1802.06002*, 2018.
- [83] Sukin Sim, Peter D Johnson, and Alán Aspuru-Guzik. Expressibility and Entangling Capability of Parameterized Quantum Circuits for Hybrid QuantumClassical Algorithms. *Advanced Quantum Technologies*, 2(12):1900070, 2019.
- [84] Ben Jaderberg, Abhishek Agarwal, Karsten Leonhardt, Martin Kiffner, and Dieter Jaksch. Minimum hardware requirements for hybrid quantum–classical DMFT. *Quantum Science and Technology*, 5(3):034015, 2020.
- [85] Lukas Mouton, Florentin Reiter, Ying Chen, and Patrick Rebentrost. Deep-learning-based quantum algorithms for solving nonlinear partial differential equations. *Physical Review A*, 110(2):022612, 2024.
- [86] Nathan Killoran, Josh Izaac, Nicolás Quesada, Ville Bergholm, Matthew Amy, and Christian Weedbrook. Strawberry Fields: A Software Platform for Photonic Quantum Computing. *Quantum*, 3:129, 2019.
- [87] Xavier Glorot and Yoshua Bengio. Understanding the difficulty of training deep feedforward neural networks. In *Proc. of the 13th Int. Conf. on Artificial Intelligence and Statistics*, pages 249–256. JMLR Workshop and Conf. Proc., 2010.
- [88] Alexander I Lvovsky. Squeezed light. *Photonics: Scientific Foundations, Technology and Applications*, 1:121–163, 2015.
- [89] Xiang-Bin Wang, Tohya Hiroshima, Akihisa Tomita, and Masahito Hayashi. Quantum information with Gaussian states. *Physics Reports*, 448(1):1–111, 2007.
- [90] PD Drummond and DF Walls. Quantum theory of optical bistability. I. Nonlinear polarisability model. *Journal of Physics A: Mathematical and General*, 13(2):725, 1980.
- [91] Zhiyuan Li, Pei Liu, Peng Zhao, Zhenyu Mi, Huikai Xu, Xuehui Liang, Tang Su, Weijie Sun, Guangming Xue, Jing-Ning Zhang, et al. Error per single-qubit gate below  $10^{-4}$  in a superconducting qubit. *npj Quantum Information*, 9(1):111, 2023.
- [92] Eric Hyppä, Antti Vepsäläinen, Miha Papič, Chun Fai Chan, Sinan Inel, Alessandro Landra, Wei Liu, Jürgen Luus, Fabian Marxer, Caspar Ockeloen-Korppi, et al. Reducing Leakage of Single-Qubit Gates for Superconducting Quantum Processors Using Analytical Control Pulse Envelopes. *PRX Quantum*, 5(3):030353, 2024.
- [93] Leon Ding, Max Hays, Youngkyu Sung, Bharath Kannan, Junyoung An, Agustin Di Paolo, Amir H Karamlou, Thomas M Hazard, Kate Azar, David K Kim, et al. High-Fidelity, Frequency-Flexible Two-Qubit Fluxonium Gates with a Transmon Coupler. *Physical Review X*, 13(3):031035, 2023.
- [94] Rui Li, Kentaro Kubo, Yinghao Ho, Zhiguang Yan, Yasunobu Nakamura, and Hayato Goto. Realization of High-Fidelity CZ Gate Based on a Double-Transmon Coupler. *Physical Review X*, 14(4):041050, 2024.

## A Loss Function Design for PDEs

### A.1 Helmholtz Equation

The Helmholtz equation represents a fundamental PDE in mathematical physics, arising as the time-independent form of the wave equation. We consider a two-dimensional Helmholtz equation of the form:

$$\begin{aligned}\Delta u(x, y) + k^2 u(x, y) &= f(x, y) & (x, y) \in \Omega \\ u(x, y) &= h(x, y) & (x, y) \in \Gamma_0\end{aligned}\quad (5)$$

where  $\Delta$  is the Laplacian operator defined as  $\Delta u = \frac{\partial^2 u}{\partial x^2} + \frac{\partial^2 u}{\partial y^2}$ ,  $k$  is the wavenumber (related to the frequency of oscillation),  $f(x, y)$  is the forcing term (source function),  $h(x, y)$  specifies the Dirichlet boundary conditions. In this study, we choose an exact solution of the form:

$$u(x, y) = \sin(a_1 \pi x) \sin(a_2 \pi y)$$

on the square domain  $\Omega = [-1, 1] \times [-1, 1]$  with Wavenumber  $k = 1$ , first mode number  $a_1 = 1$ , and the second mode number  $a_2 = 4$ . This choice of solution leads to a corresponding source term:

$$f(x, y) = u(x, y)[k^2 - (a_1 \pi)^2 - (a_2 \pi)^2]$$

To solve this problem using QCPINN, we construct a loss function that incorporates both the physical governing equation and the boundary conditions:

$$\begin{aligned}\mathcal{L}(\theta) &= \min_{\theta} (\lambda_1 \|\mathcal{L}_{\text{phy}}(\theta)\|_{\Omega} + \lambda_2 \|\mathcal{L}_{\text{bc}}(\theta)\|_{\Gamma_0}) \\ &= \min_{\theta} (\lambda_1 \text{MSE}(\underbrace{\|u_{\theta_{xx}}(x, y) + u_{\theta_{yy}}(x, y) + \alpha u_{\theta}(x, y)\|_{\Omega}}_{\text{PDE residual}}) + \text{MSE}(\lambda_2 \underbrace{\|u(x, y) - u_{\theta}(x, y)\|_{\Gamma_0}}_{\text{Boundary condition}}))\end{aligned}$$

where  $\alpha = (a_1 \pi)^2 + (a_2 \pi)^2$  combines the mode numbers into a single parameter. The chosen loss weights are  $\lambda_1 = 1.0$  and  $\lambda_2 = 10.0$ .

### A.2 Time-dependent 2D lid-driven cavity Problem

The lid-driven cavity flow is a classical CFD problem and a fundamental test case for many numerical methods, where flow is governed by the unsteady, incompressible Navier-Stokes equations. The momentum equation, continuity equation, initial condition, no-slip boundary on walls, and moving lid condition are defined, respectively, as :

$$\begin{aligned}\rho \left( \frac{\partial \mathbf{u}}{\partial t} + \mathbf{u} \cdot \nabla \mathbf{u} \right) &= -\nabla p + \mu \nabla^2 \mathbf{u} \\ \nabla \cdot \mathbf{u} &= 0 \\ \mathbf{u}(0, \mathbf{x}) &= 0 \\ \mathbf{u}(t, \mathbf{x}_0) &= 0 \quad \mathbf{x} \in \Gamma_0 \\ \mathbf{u}(t, \mathbf{x}_l) &= 1 \quad \mathbf{x} \in \Gamma_1\end{aligned}\quad (6)$$

The computational domain is  $\Omega = (0, 1) \times (0, 1)$ , the spatial discretization,  $(N_x, N_y) = (100, 100)$  is uniform grid, with temporal domain  $t \in [0, 10]$  seconds and  $\Delta t = 0.01s$  with density  $\rho = 1056 \text{ kg/m}^3$ , viscosity  $\mu = 1/\text{Re} = 0.01 \text{ kg/(m}\cdot\text{s)}$ , where Re is the Reynolds number.  $\Gamma_1$  is the top boundary (moving lid) with tangential velocity  $U = 1 \text{ m/s}$ , and  $\Gamma_0$  is the remaining three sides with no-slip condition ( $\mathbf{u} = 0$ ) where  $\mathbf{u} = (u, v)$ .

For validation purposes, we compare the neural network approximation with results obtained using the finite volume method. The PINN approach employs a composite loss function:

$$\mathcal{L}(\theta) = \min_{\theta} [\lambda_1 \underbrace{\|\mathcal{L}_{\text{phy}}(\theta)\|_{\Omega}}_{\text{PDE residual}} + \lambda_2 \underbrace{\|\mathcal{L}_{\text{up}(\theta)} + \mathcal{L}_{\text{bc}_1}(\theta)\|_{\Gamma_1 \cup \Gamma_0}}_{\text{Boundary conditions}} + \lambda_3 \underbrace{\|\mathcal{L}_{\text{u0}}(\theta)\|_{\Omega}}_{\text{Initial conditions}}]$$

where, the physics-informed loss component,  $\mathcal{L}_{\text{phy}}(\theta)$  consists of three terms:

$$\mathcal{L}_{\text{phy}}(\theta) = \mathcal{L}_{r_u} + \mathcal{L}_{r_v} + \mathcal{L}_{r_c}$$

such that:

$$\begin{aligned}\mathcal{L}_{r_u}(\theta) &= \text{MSE} \left[ (u_{\theta_t} + u_{\theta} u_{\theta_x} + v_{\theta} u_{\theta_y}) + \frac{1.0}{\rho} p_{\theta_x} - \mu(u_{\theta_{xx}} + u_{\theta_{yy}}) \right] \\ \mathcal{L}_{r_v}(\theta) &= \text{MSE} \left[ (v_{\theta_t} + u_{\theta} v_{\theta_x} + v_{\theta} v_{\theta_y}) + \frac{1.0}{\rho} p_{\theta_y} - \mu(v_{\theta_{xx}} + v_{\theta_{yy}}) \right] \\ \mathcal{L}_{r_c}(\theta) &= \text{MSE} [u_{\theta_x} + v_{\theta_y}]\end{aligned}$$

The boundary and initial conditions are enforced through the following:

$$\begin{aligned}\mathcal{L}_{\text{up}} &= \text{MSE} [(1.0 - \hat{u}) + \hat{v}] \\ \mathcal{L}_{\text{bc1}} &= \mathcal{L}_{\text{bottom, right, left}} = \text{MSE} [\hat{u} + \hat{v}] \\ \mathcal{L}_{\text{u}_0} &= \text{MSE} [\hat{u} + \hat{v} + \hat{p}]\end{aligned}$$

where,  $\mathcal{L}_{\text{up}}$  is the moving lid,  $\mathcal{L}_{\text{bc1}}$  is the no-slip walls,  $\mathcal{L}_{\text{u}_0}$  is the initial conditions. The loss weights are empirically chosen as  $\lambda_1 = 0.1$ ,  $\lambda_2 = 2.0$ ,  $\lambda_3 = 2.0$ ,  $\lambda_4 = 4.0$  for  $\mathcal{L}_{\text{phy}}$ ,  $\mathcal{L}_{\text{up}}$ ,  $\mathcal{L}_{\text{bc1}}$  and  $\mathcal{L}_{\text{u}_0}$  respectively.

### A.3 1D Wave Equation

The wave equation is a fundamental second-order hyperbolic partial differential equation that models various physical phenomena. In its one-dimensional form, it describes the evolution of a disturbance along a single spatial dimension over time. The general form of the time-dependent 1D wave equation is:

$$\begin{aligned}u_{tt}(t, x) - c^2 u_{xx}(t, x) &= 0 \\ u(t, x_0) &= f_1(t, x) \quad (t, x) \text{ on } \Gamma_0 \\ u(t, x_1) &= f_2(t, x) \quad (t, x) \text{ on } \Gamma_1 \\ u(0, x) &= g(t, x) \quad (t, x) \in \Omega \\ u_t(0, x) &= h(t, x) \quad (t, x) \in \partial\Omega\end{aligned}\tag{7}$$

where  $u(t, x)$  represents the wave amplitude at position  $x$  and time  $t$ , and  $c$  is the wave speed characterizing the medium's properties. The subscripts denote partial derivatives:  $u_{tt}$  is the second time derivative, and  $u_{xx}$  is the second spatial derivative.

For our numerical investigation, we consider a specific case with the following parameters:  $c = 2$ ,  $a = 0.5$ ,  $f_1 = f_2 = 0$ . The exact solution is chosen as:

$$u(t, x) = \sin(\pi x) \cos(c\pi t) + 0.5 \sin(2c\pi x) \cos(4c\pi t)$$

This solution represents a superposition of two standing waves with different spatial and temporal frequencies. The problem is defined on the unit square domain  $(t, x) \in [0, 1] \times [0, 1]$ , leading to the specific boundary value problem:

$$\begin{aligned}u_{tt}(t, x) - 4u_{xx}(t, x) &= 0 \quad (t, x) \in \Omega = [0, 1] \times [0, 1] \\ u(t, 0) &= u(t, 1) = 0 \\ u(0, x) &= \sin(\pi x) + 0.5 \sin(4\pi x) \quad x \in [0, 1] \\ u_t(0, x) &= 0\end{aligned}$$

To solve this problem using the proposed hybrid QCPINN, we construct a loss function that incorporates the physical constraints, boundary conditions, and initial conditions:

$$\begin{aligned}\mathcal{L}(\theta) &= \min_{\theta} [\lambda_1 \|\mathcal{L}_{\text{phy}}(\theta)\|_{\Omega} + \lambda_2 \|\mathcal{L}_{\text{bc}}(\theta)\|_{\Gamma_1} + \lambda_3 \|\mathcal{L}_{\text{ic}}(\theta)\|_{\Gamma_0}] \\ &= \min_{\theta} [\lambda_1 \text{MSE}(\underbrace{\|u_{\theta_{tt}}(t, x) - 4u_{\theta_{xx}}(t, x)\|_{\Omega}}_{\text{PDE residual}}) \\ &\quad + \lambda_2 \text{MSE}(\underbrace{\|u_{\theta}(t, 0) + u_{\theta}(t, 1) + u_{\theta}(0, x) - \sin(\pi x) - 0.5 \sin(4\pi x)\|_{\Gamma_0 \cup \Gamma_1}}_{\text{Boundary/initial conditions}}) \\ &\quad + \lambda_3 \text{MSE}(\underbrace{\|u_{\theta_t}(0, x)\|_{\partial\Omega}}_{\text{Initial velocity}})]\end{aligned}$$

The loss weights are empirically chosen as  $\lambda_1 = 0.1$ ,  $\lambda_2 = 10.0$  and  $\lambda_3 = 0.1$ .

#### A.4 Klein-Gordon Equation

The Klein-Gordon equation is a significant second-order hyperbolic PDE that emerges in numerous theoretical physics and applied mathematics areas. The equation represents a natural relativistic extension of the Schrödinger equation. In this study, we consider the one-dimensional nonlinear Klein-Gordon equation of the form:

$$\begin{aligned}
u_{tt} - \alpha u_{xx} + \beta u + \gamma u^k &= f(t, x) & (t, x) \in \Omega \\
u(t, x) &= g_1(t, x) & (t, x) \text{ on } \Gamma_0 \\
u_t(t, x) &= g_2(t, x) & (t, x) \text{ on } \Gamma_1 \\
u(0, x) &= h(t, x) & (t, x) \in \partial\Omega \times [0, T]
\end{aligned} \tag{8}$$

where  $\alpha$  is the wave speed coefficient,  $\beta$  is the linear term coefficient,  $\gamma$  is the nonlinear term coefficient, and  $k$  is the nonlinearity power. For our numerical study, we set  $\alpha = 1$ ,  $\beta = 0$ ,  $\gamma = 1$  and  $k = 3$ . We choose an exact solution of the form:

$$u(t, x) = x \cos(5\pi t) + (tx)^3$$

This solution combines oscillatory behavior with polynomial growth. The complete boundary value problem on the unit square domain becomes:

$$\begin{aligned}
u_{tt}(t, x) - u_{xx}(t, x) + u^3(t, x) &= x(-25\pi^2 \cos(5\pi t) - 6t^3) \\
&\quad + 6tx^3 + x^3(\cos(5\pi t) + t^3x^2)^3 \quad (t, x) \in \Omega = [0, 1] \times [0, 1] \\
u(t, 0) &= 0 \\
u(t, 1) &= \cos(5\pi t) + t^3 \\
u(0, x) &= x \\
u_t(0, x) &= 0
\end{aligned}$$

To solve this nonlinear PDE using the proposed QCPINN, we construct a composite loss function incorporating the physical constraints, boundary conditions, and initial conditions:

$$\begin{aligned}
\mathcal{L}(\theta) &= \min_{\theta} [\lambda_1 \|\mathcal{L}_{\text{phy}}(\theta)\|_{\Omega} + \lambda_2 \|\mathcal{L}_{\text{bc}}(\theta)\|_{\Gamma_1} + \lambda_3 \|\mathcal{L}_{\text{ic}}(\theta)\|_{\Gamma_0}] \\
&= \min_{\theta} [\lambda_1 \text{MSE}(\underbrace{\|u_{\theta_{tt}}(t, x) - u_{\theta_{xx}}(t, x) + u^3(t, x) - f(t, x)\|}_{\text{PDE residual}})_{\Omega}) \\
&\quad + \lambda_2 \text{MSE}(\underbrace{\|u(t, 0) + u(t, 1) - \cos(5\pi t) + t^3 + u(0, x) - x\|}_{\text{Boundary/initial conditions}})_{\Gamma_1}) \\
&\quad + \lambda_3 \text{MSE}(\underbrace{\|u_{\theta_t}(0, x)\|}_{\text{Initial velocity}})_{\partial\Omega})]
\end{aligned}$$

where  $f(t, x) = x(-25\pi^2 \cos(5\pi t) - 6t^3) + 6tx^3 + x^3(\cos(5\pi t) + t^3x^2)^3$ . The loss weights are chosen empirically to balance the different components as  $\lambda_1 = 1.0$ ,  $\lambda_2 = 10.0$ , and  $\lambda_3 = 1.0$ .

#### A.5 Convection-diffusion Equation

The problem focuses on solving the 2D convection-diffusion equation, a partial differential equation that models the transport of a quantity under convection (bulk movement) and diffusion (spreading due to gradients). The specific form considered here includes a viscous equation of the form:

$$\begin{aligned}
u_t + c_1 u_x + c_2 u_y - D \Delta u(t, \mathbf{x}) &= f(t, \mathbf{x}) & (t, \mathbf{x}) \in \Omega \\
u(t, \mathbf{x}_0) &= g_0(t, \mathbf{x}_0) & (t, \mathbf{x}_0) \in \Gamma_0 \\
u(t, \mathbf{x}_1) &= g_1(t, \mathbf{x}_1) & (t, \mathbf{x}_1) \in \Gamma_1 \\
u(0, \mathbf{x}) &= h(0, \mathbf{x}) & \mathbf{x} \in \partial\Omega \times [0, T]
\end{aligned} \tag{9}$$

where  $c_1$  is the convection velocity in the  $x$  direction,  $c_2$  is the convection velocity in the  $y$  direction,  $D$  is the diffusion coefficient, and  $\Delta = \frac{\partial^2}{\partial x^2} + \frac{\partial^2}{\partial y^2}$  is the Laplacian operator. For our numerical investigation, we choose an exact solution describing a Gaussian pulse:

$$u(t, x, y) = \exp(-100((x - 0.5)^2 + (y - 0.5)^2)) \exp(-t)$$

Table 4: The performance of CV-Circuit QCPINN models in solving the Helmholtz and lid-driven Cavity equations. There are 12 combinations reported in Table 1, however, results with the quadrature measurement scheme, Kerr nonlinear function, and phase-free parameterization are reported here. The remaining 11 combinations are not mentioned as the results are more or less similar.  $N_p$ : number of parameters,  $L_2$ : relative  $L_2$  error in %,  $\mathcal{L}_{\text{final}}$ : final loss. Training convergence is shown in Fig. 9.

PDE	$N_p$	$L_2$	$\mathcal{L}_{\text{final}}$
Helmholtz	469	$u$ $1.00e + 02$	5077.79
		$f$ $1.00e + 02$	
Cavity	621	$u$ $9.345e + 01$	0.102
		$v$ $9.979e + 01$	
		$p$ $8.620e + 01$	

The corresponding initial condition is:

$$h(0, x, y) = \exp(-100((x - 0.5)^2 + (y - 0.5)^2))$$

We choose  $c_1 = c_2 = 1.0$ , and  $D = 0.01$ . The complete initial-boundary value problem on the unit cube domain becomes:

$$\begin{aligned} u_t(t, x, y) + u_x(t, x, y) + u_y(t, x, y) - 0.01(u_{xx}(t, x, y) + u_{yy}(t, x, y)) &= f(t, x, y) \\ u(t, 0, y) &= \exp(-25 - 100(y - 0.5)^2 - t), \\ u(t, 1, y) &= \exp(-25 - 100(y - 0.5)^2 - t), \\ u(0, x, y) &= h(x, y) \end{aligned}$$

where  $(t, x, y) \in \Omega = [0, 1] \times [0, 1] \times [0, 1]$ ,  $f(t, x, y) = \exp(-100((x - 0.5)^2 + (y - 0.5)^2) - t)[3 - 200(x - 0.5) - 200(y - 0.5) - 400((x - 0.5)^2 + (y - 0.5)^2)]$ . To solve this problem using the proposed QCPINN model, we formulate a loss function that incorporates the physical governing equation, boundary conditions, and initial conditions:

$$\begin{aligned} \mathcal{L}(\theta) &= \min_{\theta} (\lambda_1 \|\mathcal{L}_{\text{phy}}(\theta)\|_{\Omega} + \lambda_2 \|\mathcal{L}_{\text{bc}}(\theta)\|_{\Gamma_1} + \lambda_3 \|\mathcal{L}_{\text{ic}}(\theta)\|_{\Gamma_0}) \\ &= \min_{\theta} [\lambda_1 \min(\| \underbrace{u_{\theta_t} + u_{\theta_x} + u_{\theta_y} - 0.01(u_{\theta_{xx}} + u_{\theta_{yy}})}_{\text{PDE residual}} - f \|_{\Omega}) \\ &\quad + \lambda_2 \min(\| \underbrace{u(t, 0, y) - \exp(-25 - 100(y - 0.5)^2 - t)}_{\text{Boundary conditions}} \|_{\Gamma_0}) \\ &\quad + \| \underbrace{u(t, 1, y) - \exp(-25 - 100(y - 0.5)^2 - t)}_{\text{Boundary conditions}} \|_{\Gamma_1}) \\ &\quad + \lambda_3 \min(\| \underbrace{u_{\theta}(0, x, y) - h(x, y)}_{\text{Initial conditions}} \|_{\Omega_0})] \end{aligned}$$

The loss weights are chosen to balance the different components  $\lambda_1 = 1.0$ ,  $\lambda_2 = 10.0$ , and  $\lambda_3 = 10.0$ .

## B CV-Circuit QCPINN

### B.1 Algorithm

### B.2 Results

**Helmholtz Equation.** For the Helmholtz Eq. 5, we used 469 trainable parameters. The results, in Table 4, show a high relative  $L_2$  error for both the  $u$  and  $f$  variables, along with a significant final loss. The training convergence pattern in Fig. 9(a) highlights some challenges. For example, the boundary loss, “loss\_bc”, shows a steady decrease over 10,000 iterations, suggesting that the model is gradually improving in meeting the boundary conditions. However, the residual loss, “loss\_r”, remains consistently high, with substantial fluctuations throughout the training process. This indicates that the model was struggling to satisfy the differential equation itself.

**Time-dependent 2D Lid-driven Cavity Equation.** For the more complex lid-driven Cavity Eq. 6, the CV-Circuit QCPINN model was implemented with 621 trainable parameters. The result, in Table 4, shows that the relative  $L_2$

---

**Algorithm 1** CV-Circuit QNN
 

---

**Require:** Qumodes: num\_qumodes, Layers: num\_layers, Device:  $d$ , Cutoff:  $c$ , Input: Tensor  $x$

**Ensure:** Output: Tensor  $y$

```

1: Initialize Parameters:
2:  $\psi_1, \psi_2, \phi_1, \phi_2, \phi_s, \phi_d \sim \mathcal{N}(0, 0.01\pi)$  (interferometer),  $\alpha, r \sim \mathcal{N}(0, 0.001)$ ,  $\Phi \sim \mathcal{N}(0, 0.001)$  (nonlinearity)
3: Quantum Device: Initialize  $d$  with num_qumodes, cutoff  $c$ .
4: procedure QUANTUMCIRCUIT(input)
5:   for  $i = 1$  to num_qumodes do
6:     Encode Inputs with Displacements  $D$ :  $D(\text{input}[i], 0)$  ▷ only real amplitudes
7:   end for
8:   for  $l = 1$  to num_layers do
9:     Interferometer( $\psi_1[l], \phi_1[l]$ )
10:    Squeezing( $r[l], \phi_s[l]$ ) ▷ Phase-free:  $\phi_s[l] = 0.0$ 
11:    Interferometer( $\psi_2[l], \phi_2[l]$ )
12:    Displacement( $\alpha[l], \phi_d[l]$ ) ▷ Phase-free:  $\phi_d[l] = 0.0$ 
13:    Nonlinearity  $\Phi$  ▷ Options: Kerr, Cubic Phase, Cross-Kerr
14:   end for
15:   Measure state for each wire ▷ Measurement options:  $\langle \hat{q}_i \rangle$  (Quadrature) or  $\langle \hat{n}_i \rangle$  (Number)
16:   return Measurements
17: end procedure
18: procedure INTERFEROMETER( $\psi, \phi_{bs}[l]$ )
19:   for  $l = 1$  to num_qumodes do
20:     for  $(q_1, q_2)$  in Pairs(num_qumodes) do
21:       if  $(l + k) \% 2 \neq 1$  then
22:         Beamsplitter  $B(\psi[n], \phi_{bs}[n])$  ▷ Phase-free:  $\phi_{bs}[n] = 0.0$ 
23:       end if
24:     end for
25:   end for
26:   for  $i = 1$  to num_qumodes  $- 1$  do
27:     Rotation  $R_Z(\psi[i])$ 
28:   end for
29: end procedure
30: procedure FORWARDPASS(Input  $x$ )
31:    $y \leftarrow$  QuantumCircuit( $x$ )
32:   return  $y$ 
33: end procedure

```

---

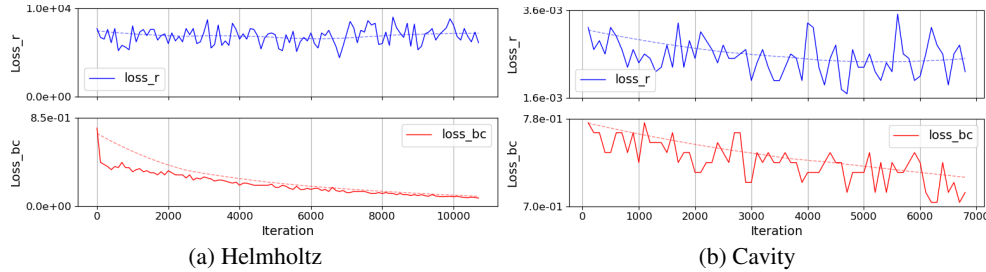


Figure 9: The training convergence of the CV-Circuit QCPINN model when solving Helmholtz and lid-driven Cavity. The terms “loss\_r” and “loss\_bc” refer to residual and boundary losses. The “loss\_bc” shows a decreasing trend, indicating improvements in satisfying the boundary conditions; however, the overall decrease is below expectation. The “loss\_r” exhibits significant fluctuations and does not display a noticeable reduction, suggesting difficulties in minimizing the residual error of the governing equation.

errors for both velocity and pressure variables remain high. However, the final loss value of 0.102 is significantly lower than that observed for the Helmholtz equation. Fig. 9(b) shows the training convergence, where the boundary loss exhibits some improvement, although it still experiences considerable fluctuations. The residual loss displays even greater oscillations compared to the Helmholtz case, indicating a greater challenge in accurately capturing the complex fluid dynamics governed by the Navier-Stokes equations.

This behavior is primarily attributed to gradient decay issues intrinsic to our CV-Circuit implementation. The vanishing gradient problem [87] manifests more severely due to the additional constraints imposed by quantum operations. Small

initialization values, while necessary to prevent divergence in quantum state evolution, significantly diminish gradients during backpropagation.

We examined various techniques, such as Xavier initialization for learnable parameters, gradient clipping, and skip connections, to mitigate the problem of gradient decay, but these attempts proved ineffective. Exploring alternative optimization strategies beyond standard gradient descent may be beneficial in addressing this issue, though this remains beyond the scope of this work.

## C DV-Circuit QCPINN

Table 5: Results from all configurations of QCPINN (DV-Circuit) models and PINN models for solving the Helmholtz equation.  $N_p$ : number of trainable parameters,  $L_2$ : relative error (in %),  $L_{\text{final}}$ : final loss, T: time per iteration (in sec), M: peak memory consumption (in MB),  $u$ : reference solution, and  $f$  source term.

	Embedding	Topology	$N_p$		$L_2$	$L_{\text{final}}$	T	M
QCPINN (DV-Circuit)	Amplitude	Alternate	772	$u$	$31.98 \pm 9.51$	$24.42 \pm 10.91$	$0.26 \pm 0.00$	$420.0 \pm 0.0$
				$f$	$7.70 \pm 1.42$			
		Cascade	771	$u$	$21.33 \pm 8.19$	$35.49 \pm 29.26$	$0.28 \pm 0.00$	$420.0 \pm 0.0$
				$f$	$8.03 \pm 2.83$			
	Cross-mesh	796	$u$	$29.39 \pm 17.84$	$23.29 \pm 16.08$	$0.31 \pm 0.0$	$440.0 \pm 0.0$	
			$f$	$7.30 \pm 3.21$				
	Layered	776	$u$	$20.95 \pm 7.46$	$18.16 \pm 9.18$	$0.29 \pm 0.03$	$420.0 \pm 0.0$	
			$f$	$4.96 \pm 0.92$				
	Angle	Alternate	772	$u$	$10.74 \pm 5.54$	$4.87 \pm 3.19$	$0.18 \pm 0.0$	$420.0 \pm 0.0$
				$f$	$3.42 \pm 0.8$			
Cascade		771	$u$	<b><math>6.69 \pm 1.51</math></b>	$4.52 \pm 1.86$	$0.17 \pm 0.00$	$420.0 \pm 0.0$	
			$f$	<b><math>2.86 \pm 0.54</math></b>				
Cross-mesh	796	$u$	$7.24 \pm 1.45$	$3.69 \pm 1.30$	$0.25 \pm 0.02$	$430.0 \pm 0.0$		
		$f$	$3.09 \pm 0.70$					
Layered	776	$u$	$18.19 \pm 10.24$	$11.63 \pm 8.73$	$0.19 \pm 0.00$	$420.0 \pm 0.0$		
		$f$	$4.88 \pm 1.42$					
PINN	Model-1		7851	$u$	$21.24 \pm 12.13$	$16.62 \pm 13.85$	$0.0041 \pm 0.0$	$340.0 \pm 0.0$
				$f$	$5.59 \pm 2.56$			
	Model-2		2751	$u$	$12.12 \pm 7.17$	$5.04 \pm 3.12$	$0.0027 \pm 0.0$	$340.0 \pm 0.0$
				$f$	$3.23 \pm 1.19$			

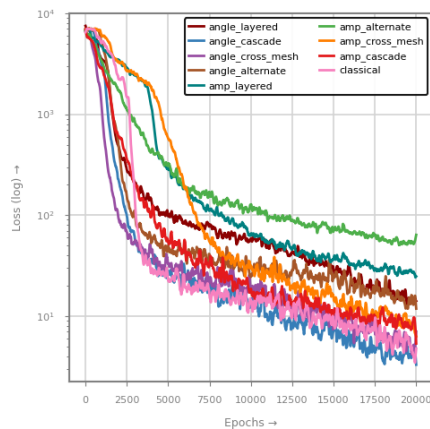


Figure 10: Training convergence history of all QCPINN (DV-Circuit) models compared to the best classical PINN model when solving the Helmholtz equation.

Table 6: Results from all configurations of QCPINN (DV-Circuit) models and PINN models for solving the Cavity problem.  $N_p$ : number of trainable parameters,  $L_2$ : relative error (in %),  $L_{\text{final}}$ : final loss, T: time per iteration (in sec), M: peak memory consumption (in MB),  $u$  and  $v$ : velocity, and  $p$ : pressure.

	Embedding	Topology	$N_p$	$L_2$	$\mathcal{L}_{\text{final}}$	T	M	
QCPINN	Amplitude	Alternate	924	$u$	$54.40 \pm 7.56$	$0.08 \pm 0.01$	$0.57 \pm 0.0$	$570.0 \pm 0.0$
				$v$	$83.07 \pm 1.04$			
				$p$	$55.53 \pm 4.38$			
		Cascade	928	$u$	$59.70 \pm 2.61$	$0.10 \pm 0.03$	$0.69 \pm 0.07$	$580.0 \pm 0.0$
				$v$	$80.15 \pm 3.38$			
				$p$	$56.44 \pm 7.54$			
	Cross-mesh	948	$u$	$39.95 \pm 0.00$	$0.07 \pm 0.00$	$0.65 \pm 0.0$	$620.0 \pm 0.01$	
			$v$	$49.62 \pm 1.10$				
			$p$	$57.13 \pm 2.00$				
	Layered	928	$u$	$59.92 \pm 3.08$	$0.09 \pm 0.03$	$0.60 \pm 0.02$	$590.0 \pm 0.0$	
			$v$	$82.67 \pm 3.33$				
			$p$	$51.92 \pm 1.99$				
Angle	Alternate	924	$u$	$26.13 \pm 2.00$	$0.05 \pm 0.00$	$0.37 \pm 0.0$	$540.0 \pm 0.0$	
			$v$	$43.86 \pm 9.00$				
			$p$	$43.86 \pm 4.10$				
	Cascade	923	$u$	$25.73 \pm 2.49$	$0.10 \pm 0.02$	$0.36 \pm 0.0$	$540.0 \pm 0.0$	
			$v$	$38.00 \pm 3.76$				
			$p$	$42.65 \pm 8.69$				
Cross-mesh	948	$u$	$27.30 \pm 4.87$	$0.08 \pm 0.03$	$0.47 \pm 0.0$	$590.0 \pm 0.0$		
		$v$	$39.88 \pm 4.58$					
		$p$	$44.99 \pm 9.24$					
Layered	928	$u$	$59.87 \pm 11.71$	$0.1 \pm 0.17$	$4.01 \pm 0.02$	$560.0 \pm 0.0$		
		$v$	$85.41 \pm 8.22$					
		$p$	$73.36 \pm 13.45$					
PINN	Model-1	8003	$u$	<b><math>21.61 \pm 6.68</math></b>	$0.06 \pm 0.02$	$0.01 \pm 0.0$	$440.0 \pm 0.0$	
			$v$	<b><math>34.24 \pm 2.76</math></b>				
			$p$	<b><math>34.82 \pm 5.25</math></b>				
	Model-2	2903	$u$	$23.03 \pm 2.45$	$0.06 \pm 0.02$	$0.01 \pm 0.0$	$435 \pm 0.0$	
			$v$	$38.81 \pm 2.73$				
			$p$	$71.51 \pm 4.79$				

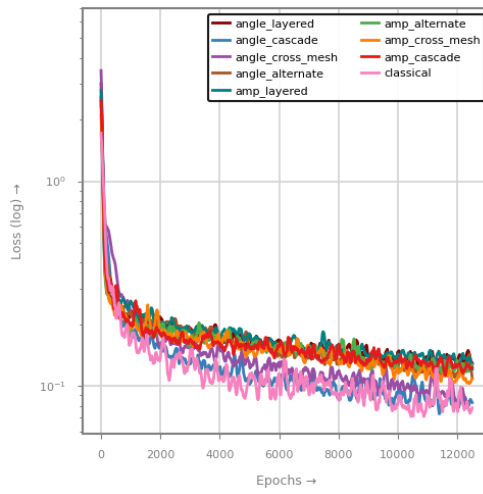


Figure 11: Training convergence history of all QCPINN (DV-Circuit) models compared to the best classical PINN model when solving the Cavity problem.

Table 7: Results from selected configurations of QCPINN (DV-Circuit) models and two PINN models.  $N_p$ : number of trainable parameters,  $L_2$ : relative error (in %),  $L_{\text{final}}$ : final loss, T: time per iteration (in sec), M: peak memory consumption (in MB),  $u$ : velocity, and  $f$ : source terms.

PDEs	Method	$N_p$		$L_2$	$\mathcal{L}_{\text{final}}$	T	M	
Wave Eq. 7	QCPINN	Angle-Alternate	772	$u$	$39.96 \pm 7.85$	$0.78 \pm 0.46$	$0.15 \pm 0.0$	$405.0 \pm 0.0$
		Angle-Layered	776	$u$	$44.76 \pm 0.28$	$1.13 \pm 0.26$	$0.17 \pm 0.0$	$419.0 \pm 0.0$
		Angle-Cascade	771	$u$	$16.74 \pm 5.41$	$0.10 \pm 0.03$	$0.25 \pm 0.06$	$446.0 \pm 0.0$
		Angle-Cross-mesh	796	$u$	$12.44 \pm 4.42$	$0.09 \pm 0.03$	$0.38 \pm 0.08$	$469.0 \pm 0.0$
	PINN	Model-1	7851	$u$	$20.94 \pm 1.70$	$0.15 \pm 0.04$	$0.02 \pm 0.03$	$353.0 \pm 0.0$
		Model-2	2751	$u$	<b><math>11.13 \pm 1.78</math></b>	$0.05 \pm 0.01$	$0.02 \pm 0.02$	$351 \pm 0.00$
Klein-Gordon Eq. 8	QCPINN	Angle-Alternate	772	$u$	$15.54 \pm 5.56$	$0.51 \pm 0.37$	$0.16 \pm 0.0$	$406.0 \pm 0.0$
				$f$	$1.99 \pm 0.96$			
		Angle-Layered	776	$u$	$14.86 \pm 4.78$	$0.51 \pm 0.41$	$0.17 \pm 0.0$	$409.0 \pm 0.0$
				$f$	$2.33 \pm 1.10$			
	QCPINN	Angle-Cascade	771	$u$	<b><math>4.24 \pm 1.88</math></b>	$0.27 \pm 0.10$	$0.25 \pm 0.03$	$447.0 \pm 0.0$
				$f$	<b><math>1.72 \pm 0.50</math></b>			
		Angle-Cross-mesh	796	$u$	$5.64 \pm 1.87$	$0.34 \pm 0.21$	$0.42 \pm 0.11$	$468.0 \pm 0.0$
				$f$	$1.65 \pm 0.38$			
PINN	Model-1	7851	$u$	$5.47 \pm 3.57$	$0.61 \pm 0.35$	$0.03 \pm 0.04$	$348.0 \pm 0.0$	
			$f$	$2.58 \pm 1.24$				
	Model-2	2751	$u$	$4.48 \pm 1.72$	$0.34 \pm 0.13$	$0.02 \pm 0.02$	$350.0 \pm 0.0$	
			$f$	<b><math>1.79 \pm 0.47</math></b>				
Convection-diffusion Eq. 9	QCPINN	Angle-Alternate	822	$u$	$5.06 \pm 2.08$	$0.001 \pm 0.001$	$0.13 \pm 0.0$	$403.0 \pm 0.0$
				$f$	$3.22 \pm 0.65$			
		Angle-Layered	826	$u$	$5.10 \pm 3.22$	$0.01 \pm 0.01$	$0.15 \pm 0.0$	$410.0 \pm 0.0$
				$f$	$3.40 \pm 1.62$			
	QCPINN	Angle-Cascade	821	$u$	$5.04 \pm 1.43$	$0.001 \pm 0.001$	$0.27 \pm 0.06$	$445.0 \pm 0.0$
				$f$	$3.03 \pm 1.00$			
		Angle-Cross-mesh	846	$u$	<b><math>4.54 \pm 2.17</math></b>	$0.001 \pm 0.001$	$0.42 \pm 0.11$	$468.0 \pm 0.0$
				$f$	<b><math>2.63 \pm 1.61</math></b>			
PINN	Model-1	7901	$u$	$12.62 \pm 6.05$	$0.02 \pm 0.02$	$0.01 \pm 0.0$	$348.0 \pm 0.0$	
			$f$	$5.57 \pm 3.05$				
	Model-2	2801	$u$	$36.80 \pm 8.79$	$0.11 \pm 0.06$	$0.01 \pm 0.0$	$346.0 \pm 0.0$	
			$f$	$21.27 \pm 8.12$				

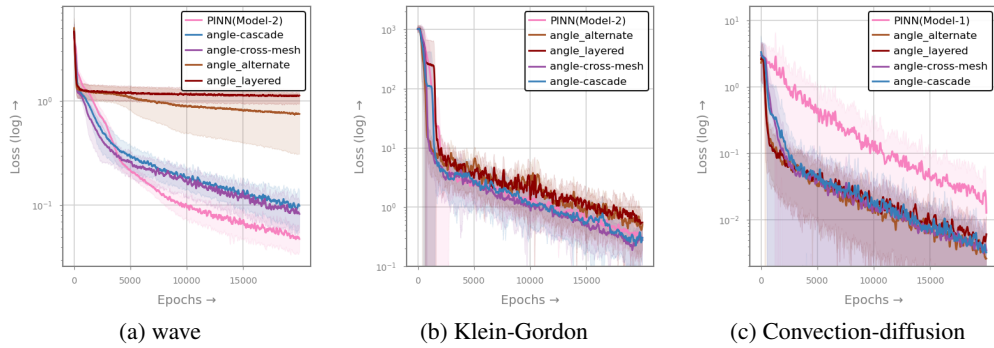


Figure 12: Each plot compares the convergence behavior of the QCPINN models with angle embedding with the best-performing classical PINN model.